Measurement 202 (2022) 111759

Contents lists available at ScienceDirect

Measurement

journal homepage: www.elsevier.com/locate/measurement

Deep learning CNN-LSTM-MLP hybrid fusion model for feature optimizations and daily solar radiation prediction

Sujan Ghimire [a], Ravinesh C. Deo [a], David Casillas-Pérez [b,*], Sancho Salcedo-Sanz [a,c], Ekta Sharma [a], Mumtaz Ali [d,e]

[a] School of Mathematics, Physics and Computing, University of Southern Queensland, Springfield, QLD, 4300, Australia
[b] Department of Signal Processing and Communications, Universidad Rey Juan Carlos, Fuenlabrada, 28942, Madrid, Spain
[c] Department of Signal Processing and Communications, Universidad de Alcalá, Alcalá de Henares, 28805, Madrid, Spain
[d] Deakin-SWU Joint Research Centre on Big Data, School of Information Technology, Deakin University, VIC 3125, Australia
[e] UniSQ College, University of Southern Queensland, Springfield, QLD, 4300, Australia

ARTICLE INFO

MSC:
68T05
68T20

Keywords:
Global solar prediction
Deep Learning networks
Convolutional Neural Networks
Slime Mould Algorithm
Renewable energy
Global climate models

ABSTRACT

Global solar radiation (GSR) prediction plays an essential role in planning, controlling and monitoring solar power systems. However, its stochastic behaviour is a significant challenge in achieving satisfactory prediction results. This study aims to design an innovative hybrid prediction model that integrates a feature selection mechanism using a **S**lime-Mould algorithm, a **C**onvolutional-Neural-Network (CNN), a **L**ong–Short-Term-Memory Neural Network (LSTM) and a final CNN with Multilayer-Perceptron output (SCLC algorithm hereafter). The proposed model was applied to six solar farms in Queensland (Australia) at daily temporal horizons in six different time steps. The comprehensive benchmarking of the obtained results with those from two Deep-Learning (CNN-LSTM, Deep-Neural-Network) and three Machine-Learning (Artificial-Neural-Network, Random-Forest, Self-Adaptive Differential-Evolutionary Extreme-Learning-Machines) models highlighted a higher performance of the proposed prediction model in all the six selected solar farms. From the results obtained, this work establishes that the designed SCLC algorithm could have a practical utility for applications in renewable and sustainable energy resource management.

1. Introduction

There is unprecedented momentum to leave fossil fuel age behind us. With the rapid transition to renewable energy and energy efficiency, the Governments globally are trying to leave the fossil fuel age for a more sustainable development paths and lower emissions [1–4]. Solar energy carries the potential to fulfil the entire world's energy needs and relieve the current world energy crisis [5–8]. It is an inexhaustible, clean, renewable energy source [9]. Being a sustainable, and infinite energy source, solar energy carries the potential to fulfil the energy needs of the entire world. Global solar radiation (*GSR*) identifies the solar power potential [10]. An accurate *GSR* prediction is very important for an effective solar energy utilization, robust planning, decision making, power system operation, management, and investment applications [11]. Furthermore, accurate *GSR* predictions are vital for the establishment of reliability and permanency of the electricity grid, and the reduction of risk and costs of energy markets and systems. This will be immensely beneficial not only to the power plants and grid operators but also to traders and Government policymakers [12].

Many researchers have proposed different models to predict *GSR*, including empirical prediction models (EM) [13–17]. EM are computationally efficient and easy to calculate, but because of rapid changes in weather conditions, they cannot, in general, accurately predict short-term GSR [18]. In many cases, they result in partially unsatisfactory estimates of GSR [19–22]. Physical [23,24] and Numerical Weather Prediction (NWP) [25,26] are other types of GSR prediction models quite studied in the literature. Problems like choosing input for the physical or the NWP models with phenomenal cost of computations exist here [27–29]. There are other types of approaches for *GSR* prediction such as remote sensing retrieval [30], time series-based algorithms [31,32] and, of course, Machine Learning (ML)-based models.

GSR prediction popularly benefits from the usage of machine learning techniques such as Artificial Neural Networks (ANN). This includes Multilayer Perception Neural Networks (MLP-NNs) [33–35], recurrent

* Corresponding author.
E-mail addresses: sujan.ghimire@usq.edu.au (S. Ghimire), ravinesh.deo@usq.edu.au (R.C. Deo), david.casillas@urjc.es (D. Casillas-Pérez), sancho.salcedo@uah.es (S. Salcedo-Sanz), ekta.sharma@usq.edu.au (E. Sharma), mumtaz.ali@deakin.edu.au (M. Ali).

https://doi.org/10.1016/j.measurement.2022.111759
Received 25 April 2022; Received in revised form 4 August 2022; Accepted 13 August 2022
Available online 19 August 2022

neural networks [36], Radial Basis Function Neural Networks (RBF-NNs) [37], evolutionary neural approaches [38,39] Generalized Regression Neural Networks (GR-NNs) [40], or Extreme Learning Machines (ELM) [41–44], among others. Several other popular choices for the *GSR* prediction are Random Forest (RF) Regression (RFR) [45,46], Support Vector Regression algorithms (SVR) [47–50], Gaussian Processes [51] and Adaptive Neuro-Fuzzy Inference System (ANFIS) [52]. Studies in the past have taken the comparison of different ML techniques in *GSR* prediction. For e.g. the authors of, such as [53] have used SVR, ELM, and MLP for their *GSR* prediction. Authors of [54] uses EM, ANN, SVR, Gaussian Process, Genetic Programming (GP), and ARIMA models for *GSR* prediction in the Australian cities. Several mathematical models were used for the time series with EM and ANNs [55]. However, in a study in Mexico, three different algorithms such as ANFIS, ANN, and SVM were used by the authors of [56] for their problem. In the study [50], the authors used only a few variables such as temperature, hours of sunshine, evaporation etc with the SVR model based on wavelets for forecasting the solar radiation.

On the other hand, Deep Learning (DL) is gaining huge popularity from the past decade. This is due to their robust architecture, powerful nonlinear structure, generalization capability, and unsupervised feature learning. Unlike shallow ML models, DL models can extract features and latent invariant architectures in data. This makes them a popular choice for areas such as imaging, speech recognition, natural language processing, autonomous driving, or computer vision. Solar prediction with DL technologies is a new and promising research area [57]. Deep learning models such as LSTM have been taken into consideration to predict hourly solar radiance for the next day [58,59], while other popular models such as CNN picks up variables and chooses key features for *GSR* [60]. The authors of [61] merged various attention mechanisms with the Gated Recurrent Unit (GRU). In [62] a comparison of machine learning methods, such as, polynomial regression, SVRs, ANNs and RF; and deep learning algorithms, such as CNNs and RNNs, is developed for predicting GSR. [63] chooses to use techniques such as Embedded Clustering (ECs) with the Deep Belief Networks (DBNs) for solar irradiance. However, the Bidirectional LSTM network, along with Sine Cosine Algorithm (SCA) was chosen with the Complete Ensemble Empirical Mode Decomposition with Adaptive Noise (CEEMDAN) by the authors of [64] to predict *GSR* prediction. Considering the study that optimizes various deep learning techniques such as LSTM, GRU, and RNN, the authors of [65] proposes a genetic algorithm (GA). In [66] study conducted in Finland, the power of deep learning hybrids have again been explored through Choquet Integrals based functions of aggregation with LSTM. Latter was also used with the ResNet (Residual Network) by the authors [67] to make hybrid model for short *GSR* predictions. More recently, forecasting methods based on Global Horizontal Irradiance (GHI) [68] are proposed. In [69] two hybrid DNN models for hourly GSR prediction in Africa have been discussed and compared. DNN-based models for hybridization, specifically CNNs, are also used in combination with empirical mode decomposition approaches [70,71], traditional ML [72–74] or ensemble methods [75,76], including different feature selection techniques for GSR prediction.

As previously discussed, the single model usage in modelling has disadvantages of intermittent and fluctuating nature of *GSR*. Due to the shortcomings of single models and the need for greater accuracy in *GSR* prediction, hybrid models have been developed and widely used for predicting *GSR*. However, there are some concerns of these hybrid models too: First, in most studies *GSR* is the only factor considered (or clear sky data taken) during model development, ignoring meteorological factors. In practicality, as the weather varies significantly, these models cannot fully reflect the change in *GSR*. Second, the weather forecast becomes more accurate and convenient, it gets rarely modelled with hybrid models as input parameters. Third, feature selection algorithms are not solely preferred during the modelling process of these hybrid models. It is important to note that, although the resultant hybrid of deep fusion network benefits from both DL and ML, it should alleviate the drawbacks of both the techniques such as computation time and cost. Hybrid models provide more accurate and less computationally expensive solutions when used through Tensorflow, which is Google's open-source platform [77]. Most published literature for *GSR* fails to address these criteria. These are some of the gaps the present study attempts to address.

This paper therefore proposes a novel DL-based hybrid model that overcomes the above limitations, and produces accurate *GSR* predictions. A new hybrid DL model, which process the input data with a sequential application of Slime Mould Algorithm (SMA) for feature selection, CNN, LSTM network, CNN and a final processing with a MLP has been developed in this study, to overcome the shortcomings mentioned above and obtain a more accurate *GSR* prediction. The complete prediction system is called SCLC, and we have tested it by comparison with an ensemble of two alternative DL approaches (CNN-LSTM and Deep Neural Network (DNN)) and three shallow ML models (Artificial Neural Network, Random Forest and a variation of the Extreme Learning Machine).

The rest of this study is as follows: next section summarizes the different methods which form the SCLC prediction system, including, the SMA, CNN and LSTM algorithms. The data and area of the experimental study are described in Section 2.1. The hybrid SCLC model description and tuning is presented in Section 2.3. The experimental part and results obtained are summarized in Section 3. In the end, the study discusses the results in the form of conclusions in Section 4.

2. Methodology

2.1. Study area and data

Queensland is renowned for being a leader in the Australian solar revolution. With high solar radiation, the region of Western Downs has gained a lot of recognition for its pro-solar movements. Currently, the state of Queensland generates $9.9 billion in investments through 44 enormous projects of renewable energy, generating 5156 megawatts, and 7000 jobs in construction [78]. This saves about 12 million tons of carbon annually. Including rooftop solar panels, the state of Queensland promises the renewable energy capacity of 6200 MW, accounting 20% of total electricity consumption [79]. Australia with The power outputs selected for the study varies from 55 MW to 148 MW.

1. The Cape York Battery Power Plant is the first grid-connected battery power plant in Australia with both solar generation and battery storage. According to the developer, the 20 MW/80 MWh Fluence battery-based energy storage system plus 55 MW solar generation will provide firm clean energy through a single connection point, using a single power plant controller.
2. The Chinchilla Solar Farm is situated 140 km north of Toowoomba, Australia, near the township of Chinchilla. There will be around 250,000 thin-film photovoltaic (PV) modules installed at the proposed 100 MW project and they will produce enough solar energy to serve approximately 40,000 average Queensland homes.
3. Sun metal solar Farm possesses a 125 MW generation capacity and is located near Townsville, in northern Queensland. Sun Metals is building the farm to secure their zinc refinery there with an uninterruptible power supply for a lower cost. A total of 1,167,000 solar panels are used and will produce 261 GWh of electricity annually, which accounts for almost 29% of the zinc refinery's current electrical needs.
4. Clermont Solar Farm would build a single-axis tracking solar power plant, located 106 km north-northeast of Emerald, Queensland. In total, the site can generate approximately 89 MW and encompasses approximately 497 acres. A total of 205 GWh of electricity will be generated annually using 275,442 PV panels, enough to power approximately 30,996 households.

Table 1
Descriptive statistics of the target variable: daily global solar radiation (*GSR*; $MJm^{-2}day^{-1}$) for six solar farms in Queensland, Australia.

Property	Barunggam	Cameby	Cape York Solar Storage	Chinchilla	Clermont	Sun Metals
Latitude	26.685°S	26.682°S	15.898°S	26.670°S	22.839°S	19.437°S
Longitude	150.765°E	150.510°E	144.857°E	150.793°E	147.581°E	146.696°E
Capacity (MW)	140	148	55	100	75	125
Median (MJm^{-2})	19.00	19.00	20.00	19.00	20.00	20.00
mean (MJm^{-2})	19.23	19.28	19.45	19.21	20.03	19.88
Standard deviation (MJm^{-2})	6.36	6.43	4.84	6.35	5.85	5.55
Variance (MJm^{-2})	40.49	41.34	23.38	40.27	34.18	30.77
Maximum (MJm^{-2})	33.00	32.00	29.00	32.00	32.00	31.00
Minimum (MJm^{-2})	4.00	4.00	5.00	4.00	4.00	4.00
Mode (MJm^{-2})	29.00	28.00	24.00	28.00	28.00	27.00
Interquartile range (MJm^{-2})	9.00	9.00	6.00	9.00	8.00	7.00
Skewness	−0.18	−0.18	−0.51	−0.18	−0.38	−0.54
Kurtosis	2.34	2.34	2.83	2.35	2.65	2.71

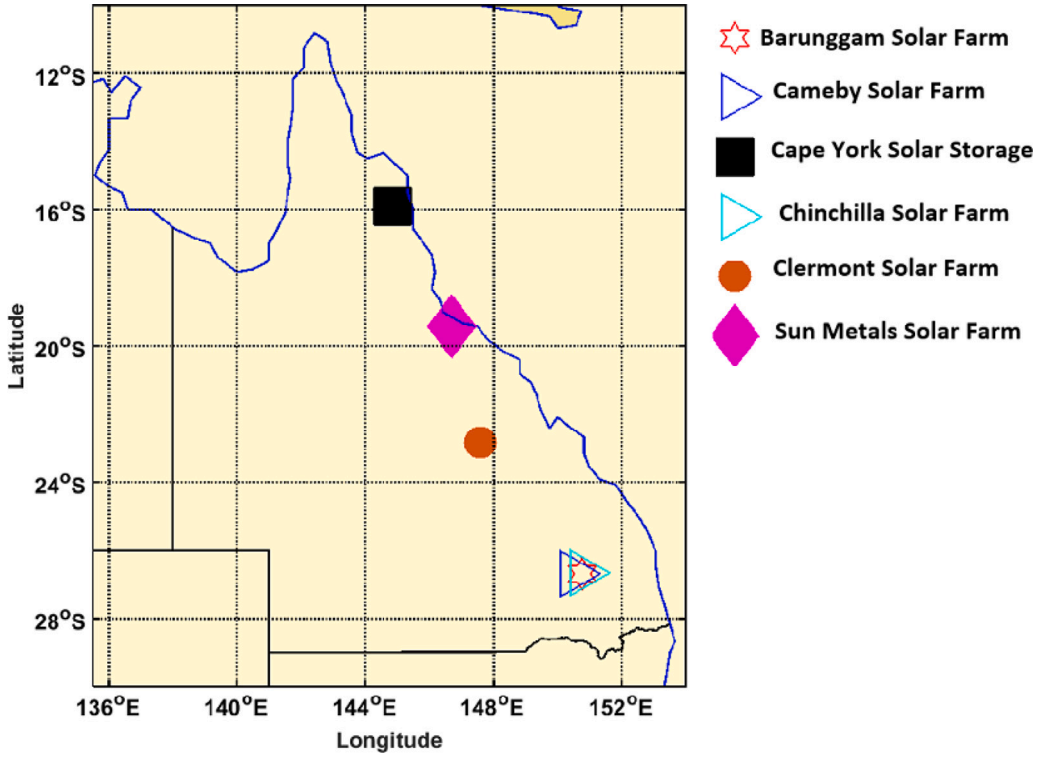

Fig. 1. Study sites in Queensland, Australia, where the proposed deep hybrid SCLC model was implemented.

5. Ubergy has received approval for its Barunggam Solar Farm located on Baking Board, 14 km from Chinchilla in Queensland. This solar farm is expected to be 140 MW in size.
6. Cameby solar farm will have a capacity of 148 MW and is located in an area of 463ha that presently serves as grazing land with little agricultural potential.

Moreover, it supports the Queensland government's goal of producing 50 percent of its energy from renewable sources by 2030, while establishing Queensland as a leader in renewable energy. Table 1 provides details of the region of study with *GSR*) statistics and Fig. 1 depicts their locations.

A supervised learning process is one in which an example input (predictor) and the desired output (predictand) are presented to a predictive model, for instance *GSR* prediction, as there is a need of both predictors and predictands. The predictions in this study are based on the meteorological data in the form of global climate models (GCM), Scientific Information for Landowners (SILO) data regarding ground-based values. A part of the Department of Science, Information Technology, Innovation and the Arts (DSITIA) is a body Queensland Climate Change Centre of Excellence (QCCCE) managing the Long Paddock SILO database [80]. A GCM archive is maintained by The Centre for Environmental Data Analysis (CEDA) [81]. Daily atmospheric model outputs for the historical are sourced from this repository. The models include CSIRO-BOM ACCESS1-0 (grid size 1.25° × 1.875°) [82], MOHC Hadley-GEM2-CC (grid size 1.25° × 1.875°) [83] and the MRI MRI-CGCM3 (grid size 1.12148° × 1.125°) [84]. The GCM model outputs are indexed by dimensions of longitude, latitude, time, atmospheric pressure (at 8 levels), or near-surface readings. The historical outputs span the period 1950-01-01T12:00:00 to 2006-01-01T00:00:00. Table 2 illustrates the variables of meteorology used by the study that had 20455 records and 75 meteorological variables (20455 × 75).

2.2. *Theoretical overview*

To predict solar radiation, the study provides a brief theoretical description of the several techniques that form the SCLC system. It first describes the SMA approach for feature selection and then describe the foundations of the CNN algorithm and the LSTM approach.

Table 2
Description of the global pool of predictor variables used in daily *GSR* prediction.

Data repository name	Variable	Description	Units
Global Circulation Model (GCM) Atmospheric Predictor Variables	clt	Cloud area fraction	%
	hfls	Surface upward latent heat flux	wm^{-2}
	hfss	Surface upward sensible heat flux	wm^{-2}
	hur	Relative humidity	%
	hus	Near surface specific humidity	gkg^{-1}
	pr	Precipitation	$kgm^{-2}s^{-1}$
	prc	Convective precipitation	$kgm^{-2}s^{-1}$
	prsn	Solid precipitation	$kgm^{-2}s^{-1}$
	psl	Sea level pressure	pa
	rhs	Near surface relative humidity	%
	rhsmax	Surface daily max relative humidity	%
	rhsmin	Surface daily min relative humidity	%
	sfcWind	Wind speed	ms^{-1}
	sfcWindmax	Daily maximum near-surface wind speed	ms^{-1}
	ta	Air temperature	K
	tas	Near surface air temperature	K
	tasmax	Daily max near-surface air temperature	K
	tasmin	Daily min near-surface air temperature	K
	ua	Eastward wind	ms^{-1}
	uas	Eastern near-surface wind	ms^{-1}
	va	Northward wind	ms^{-1}
	vas	Northern near-surface wind	ms^{-1}
	wap	Omega (Lagrangian tendency of air pressure)	pas^{-1}
	zg	Geopotential height	m
Ground-based SILO	T.Max	Maximum temperature	K
	T.Min	Minimum temperature	K
	Rain	Rainfall	mm
	Evap	Evaporation	mm
	VP	Vapour pressure	Pa
	RHmaxT	Relative humidity at maximum temperature	%
	RHminT	Relative humidity at minimum temperature	%

2.2.1. Slime Mould Algorithm for feature Selection

In this study, a wrapper feature selection method [85–87] based upon a meta-heuristic algorithm called Slime Mould Algorithm (SMA) is firstly used to select the optimal features for *GSR* prediction. We have selected SMA based on its recent performance as a metaheuristic algorithm derived from the diffusion and foraging behaviour of slime mould [88]. Mathematically, SMA can be divided into three phases: approach, wrap and grabble food.

- Stage 1 (Approach food): A slime mould approaches food based on its odour in the air, so the following formula mimics the behaviour of the slime mould towards food.

$$\mathbf{X}(t+1) = \begin{cases} \mathbf{X}_b(t) + v_b\left(W\mathbf{X}_A(t) - \mathbf{X}_B(t)\right), & r < p \\ v_c\mathbf{X}(t), & r \geq p \end{cases} \tag{1}$$

where the slime mould position is denoted by $\mathbf{X}$, and $\mathbf{X}_b$ shows the position of current individual. The notation a is calculated as Eq. (2):

$$a = \operatorname{arctanh}\left(-\frac{t}{M_t} + 1\right), \tag{2}$$

where t is the current iteration and M_t is the maximum iterations; and p is derived by Eq. (3):

$$p = \tanh|S(i) - DF|. \tag{3}$$

Here, $i \in \{1, 2, \ldots, n\}$ and $S(i)$ denotes the fitness of $\mathbf{X}$. DF represents a good fitness iteration. The weight of slime mould W is calculated following the next expression:

$$W(SI(i)) = \begin{cases} 1 + r\log\left(\frac{bF - S(i)}{bF - wF} + 1\right), & \text{if } S(i) < \text{Med}[S] \\ 1 - r\log\left(\frac{bF - S(i)}{bF - wF} + 1\right), & \text{otherwise} \end{cases}, \tag{4}$$

where

$$SI = \text{Sort}[S], \tag{5}$$

and $r \sim U(0,1)$ is an uniform random variable between 0 and 1. The Med[·] refers to the median operator.

- Stage 2 (Wrap food): A slime mould's search pattern changes based on the quality of food. When there is a high concentration of food near a region, the weight near it will be greater. If the concentration is low, the region's weight will be lower, and it will be forced to explore other locations. The location of the slime mould is updated in the stage based on Eq. (6):

$$\mathbf{X}(t+1) = \begin{cases} u(UB - LB) + LB, & r < z \\ \mathbf{X}_b(t) + v_b\left(W\mathbf{X}_A(t) - X_B(t)\right), & z \leq r < p \\ v_c\mathbf{X}(t), & r \geq p \end{cases} \tag{6}$$

where LB and UB are the lower and upper bounds respectively, $u, r \sim U(0,1)$, and z is a probability used to tradeoff between exploitation and exploration.

- Stage 3 (Grabble food): Here, slime mould moves to better locations for food concentration. W, v_b and v_c is used to mimic the variation of venous width. The variables, v_b and v_c, oscillate between $[-a, a]$ and $[-1, 1]$ respectively. As the iteration number increases, v_b and v_c draw closer to zero. The intuitive and detailed process of SMA is shown in Fig. 2.

Since, this SMA is wrapper-based method, to implement the SMA algorithm for feature selection, a learning algorithm must be incorporated. This study has utilized K-Nearest Neighbours (KNN) regressor [89] as a learning algorithm for the feature selection (FS) using SMA. The objective of FS is to increase the accuracy while also minimizing the number of features to be selected, therefore, we have chosen fitness value (FV) as the root mean square error (RMSE) complement of regression accuracy and needs to be minimized to get the best feature subset. The three phases of the proposed SMA based FS solution are outlined below:

- Initialization Phase: A SMA produces an initial population of N candidate solutions, where each entity covers a set of features for consideration. The quality and convergence of the optimal

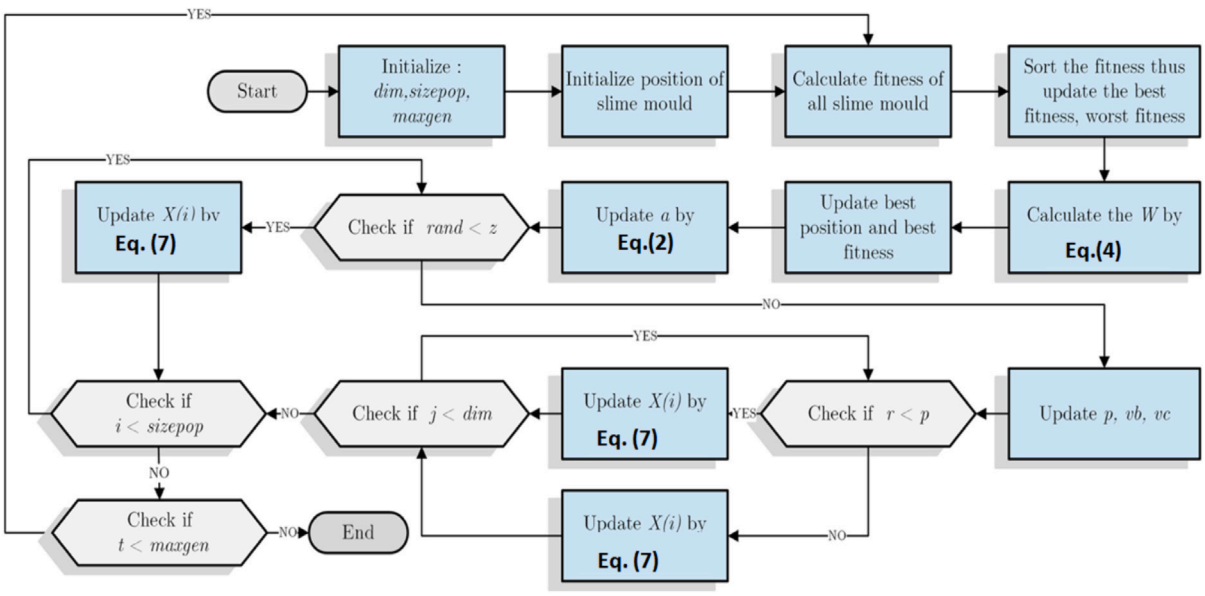

Fig. 2. Descriptive flowchart for the relevant steps in the Slime Mould Algorithm (SMA) adopted as a feature selection algorithm for the prediction of *GSR*.

solution are critically affected by this step. The population X_0 is randomly generated by Eq. (1), and the fitness value is calculated.

- Update Phase: Every new position is evaluated using the fitness function. If the solution quality of a new position is better than that of the current position, the position is updated. The opposite-based learning (OBL) approach [90] is used to update each search agent's position, Eqs. (4) and (6) are used. To improve the search process by exploring new regions in quest of the optimal solution, increasing algorithm diversity, avoiding local optima, and confirming whether the new solution is better than the old one, the basic principle of OBL is to consider a solution and its matching opposite solution simultaneously. The FV of the new population is calculated, and then the best solution is determined. Repetition of this process will continue until the termination condition (*i.e.*, the maximum number of function evaluations) is reached. The SMA process returns the best solution obtained in the previous step and only the best features are retained from the original data.
- Termination phase: Until the stopping criteria are satisfied, the maximum number of function evaluations of the proposed algorithm are performed, and the best viable feature subset is discovered.

2.2.2. Convolutional Neural Network (CNN)

CNN models are a popular choice of the feed-forward network since CNN shares features parameters and enable dimensionality reduction. As CNN enables parameter sharing, the number of parameters gets reduced therefore the computations are also decreased. Compared to its predecessors, the main advantage of CNN is that it automatically detects important spatial features without any human supervision. The convolution layers of a CNN are optimized during training so that they extract highly discriminative features, while the latter layers resemble multilayer perceptron's which execute classifying or regression work. Although CNN is very popular, still there have been very few papers describing the application of CNNs for solar radiation modelling [91]. Fig. 3 shows the structure of CNN, which consists of an input layer, convolution layer, pooling layer, full connection layer, and an output layer [92].

A convolutional neural network has two main features: weight sharing and local connections [93]. Convolutional layers target meteorological data as input variables with strata on the target variable (*GSR*) to extract spatial patterns, which can be expressed mathematically as:

$$h = f(x * W + b) \tag{7}$$

where x is input data, $*$ means convolution operation, W is the weight of the convolution kernel, and b is the offset value. The function $f(\cdot)$ denotes the activation function. Rectified linear unit (ReLu), is the chosen activation function for this study:

$$f(x) = \max\{0, x\} \tag{8}$$

2.2.3. Long Short-Term Memory Network (LSTM)

Relative insensitivity to gap length is an advantage of LSTM over RNNs, hidden Markov models, and other sequence learning methods in numerous applications. LSTMs were developed to deal with the vanishing gradient problem that can be encountered when training traditional RNNs. Using LSTM, time series forecasting models can predict future values based on previous, sequential data. This provides greater accuracy for demand forecasters which results in better decision-making for the business. We can say that, when we move from RNN to LSTM (Long Short-Term Memory), we are introducing more and more controlling knobs, which control the flow and mixing of Inputs as per trained Weights. And thus, bringing more flexibility in controlling the outputs.

Different versions of conventional neural networks are used to analyse time-series data, forecast, and predict trends. Neural networks are unable to handle historical data dependencies. Thus, there were Recurrent Neural Networks (RNN) that utilize the message gathered in the earlier. RNNs handle dependencies that are short-term, but not long-term dependencies. There are issues with vanishing and explosion of gradient.

This problem was solved through LSTM [94] that uses special cells and not neurons. Moreover, there are three gates named input, forget, and output enabling updating and controlling the information flow within the network. There are many advantages of using an LSTM. They key being gradient vanishing, other being effectively handling the internal cells. Next being efficiently handling long-term dependencies by acquiring the temporal features from time-series data. All of this makes LSTM a popular choice amongst researchers for predicting *GSR* [58,95–97]. The Fig. 4 shows the LSTM architecture. The study explains it mathematically as [98]:

- Forget gate, based on The earlier input data x_t, hidden state h_{t-1}, and the forget gate f_t decides the forget gate. This tells the LSTM to decide any specific information that it wishes to remove:

$$f_t = \sigma(w_f \cdot [h_{t-1}, x_t] + b_f) \tag{9}$$

where the weight matrices is denoted by w_f, σ represents the activation function sigmoid, and the bias vector is denoted by b_f.

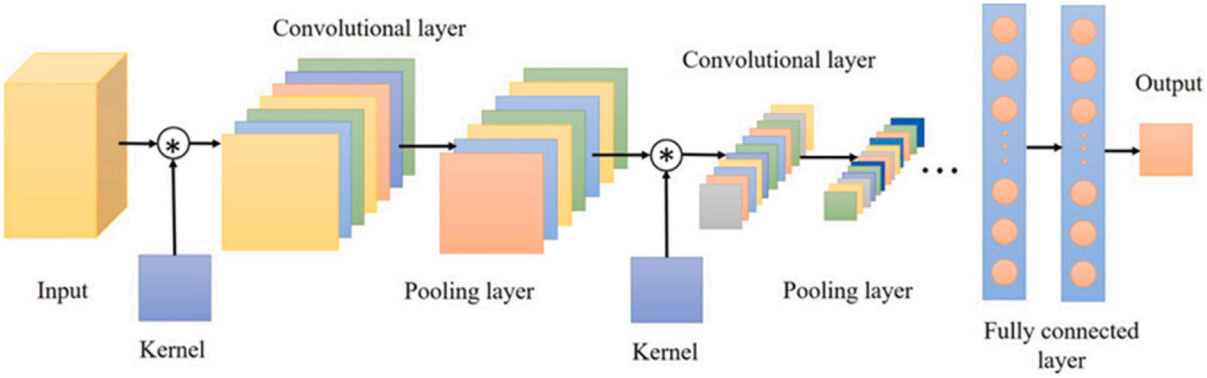

Fig. 3. A basic architecture of a Convolutional Neural Network (CNN) model.

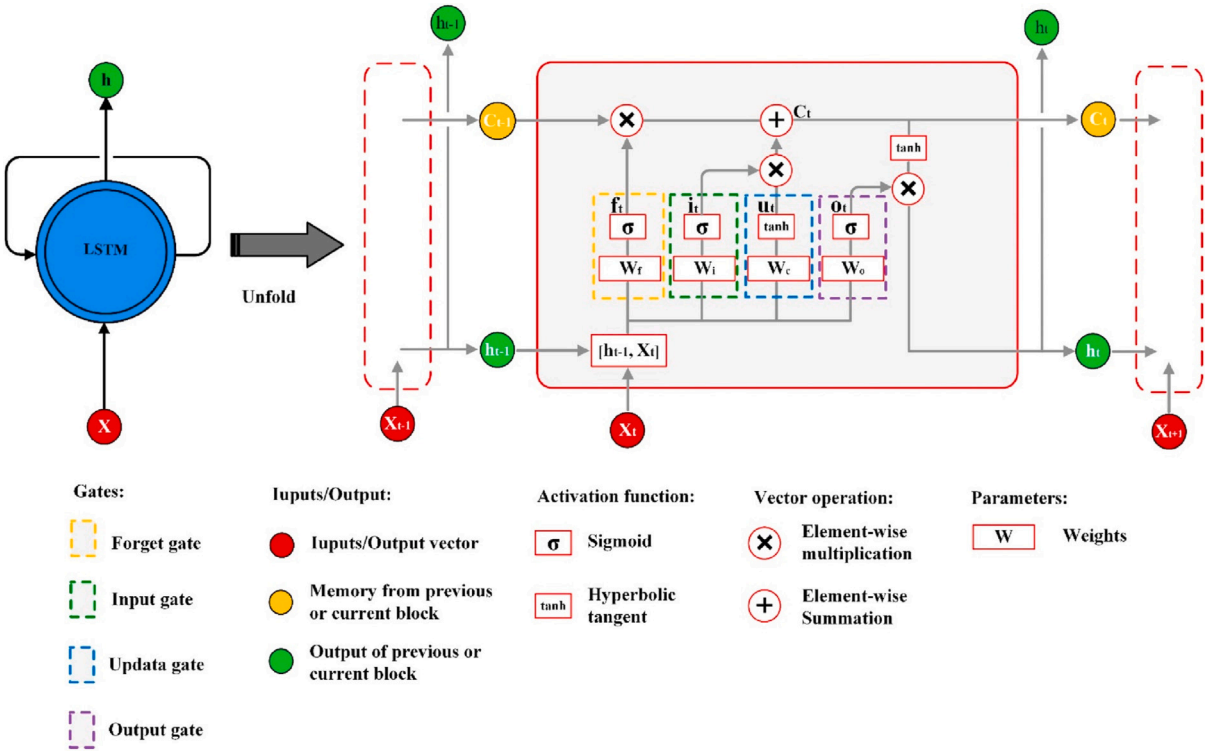

Fig. 4. The structure of Long–Short Term Memory (LSTM) Network.

- The information saved for the new candidate state $\tilde{C}_t$ is determined by the i_t, which is the input gate:

$$\tilde{C}_t = \tanh(w_c \cdot [h_{t-1}, x_t] + b_c) \tag{10}$$

$$i_t = \sigma(w_i \cdot [h_{t-1}, x_t] + b_i) \tag{11}$$

where the hyperbolic tangent function (hyperbolic) is denoted by $\tanh(\cdot)$.

- The new candidate state denoted by $\tilde{C}_t$ with the earlier state denoted by the C_{t-1} updates the next state, C_t. This is mathematically expressed as follows:

$$C_t = f_t * C_{t-1} + i_t * \tilde{C}_t \tag{12}$$

- Lastly, the output of the LSTM cell is regulated by o_t gate. In the following equation, o_t is the output gate, the cell state is C_t, and $\tanh$ is the activation function. The h_t is the desired output represented by:

$$o_t = \sigma(w_o \cdot [h_{t-1}, x_t] + b_o) \tag{13}$$

$$h_t = o_t \tanh(C_t) \tag{14}$$

2.3. The hybrid SCLC model development

The general method for predicting *GSR* introduced in this study is illustrated in Fig. 6.

In comparison to a standalone model, a hybrid model generally has a good performance. Considering the usefulness of LSTMs and CNNs, this study has proposed a new functional model for extracting temporal and spatial features to predict *GSR* with greater accuracy. In this study, a hybrid model, called Hybrid SCLC referred to as a connection of LSTM, SMA, and CNN is proposed to model daily *GSR*, as illustrated in Fig. 5. The objective model predicts *GSR* through extraction of difficult patterns from the data. The model is developed in the following stages:

- Stage 1: Initially, the complete meteorological data was used for *GSR* prediction.

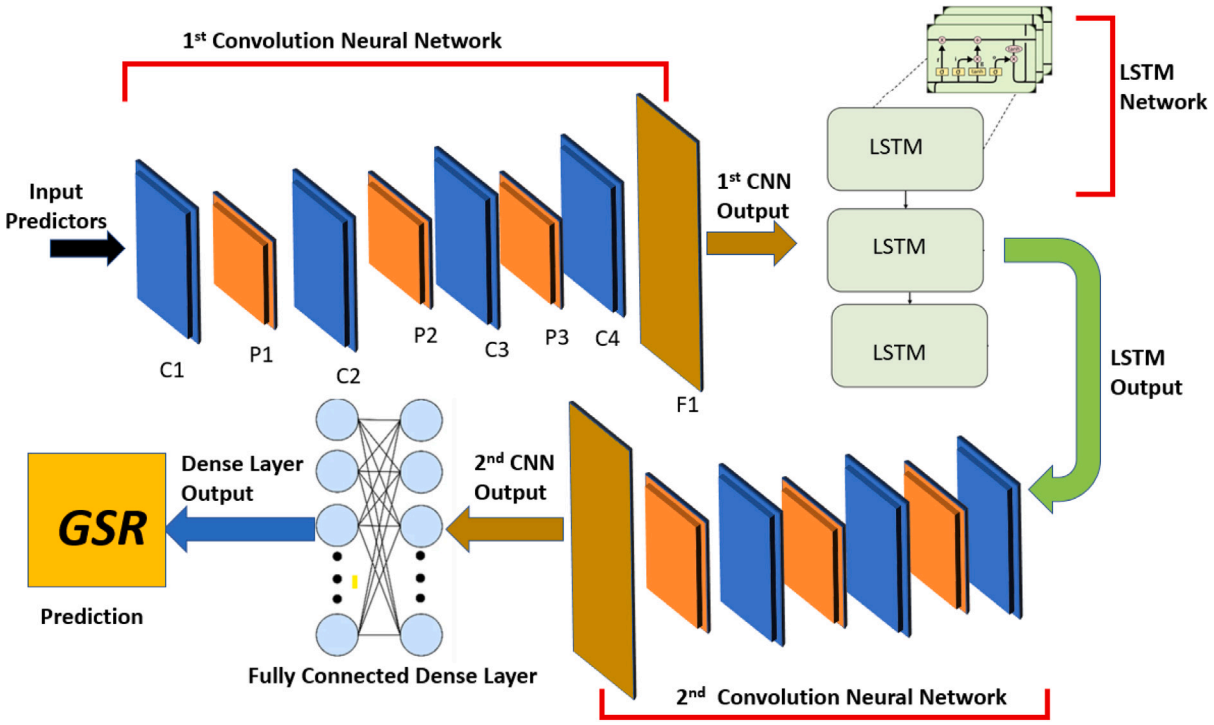

Fig. 5. Architecture of the proposed *GSR* prediction method based on the hybrid SMA-CNN-LSTM-CNN-MLP (SCLC) model.

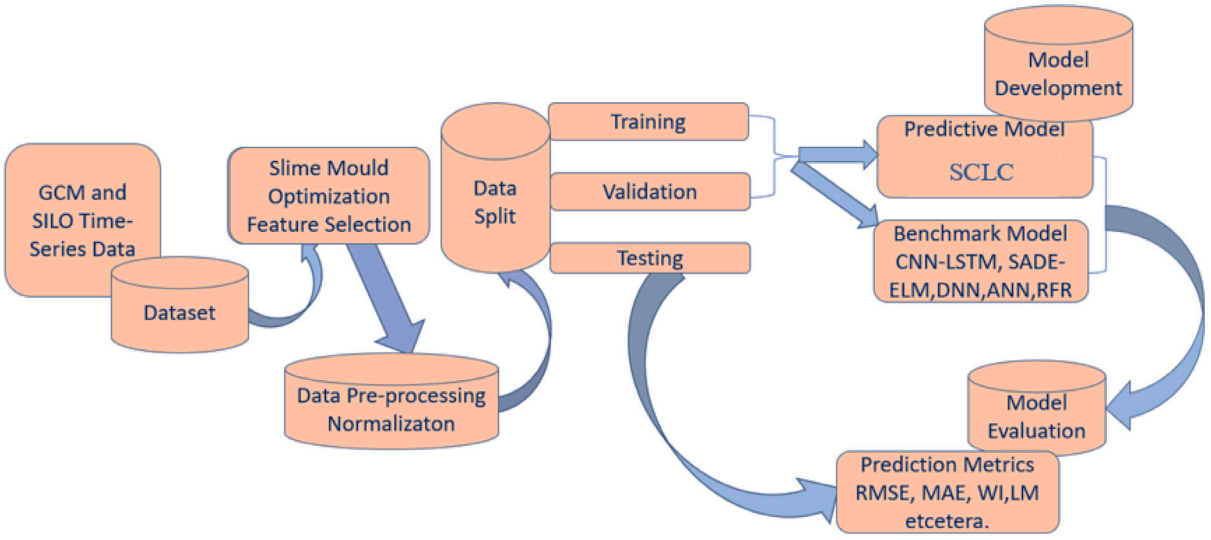

Fig. 6. Workflow diagram detailing the necessary steps taken to design proposed deep hybrid SCLC model.

- Stage 2: Secondly, Slime Mould Algorithm was adopted as a stochastic optimizer in the study to extract features. The proposed SMA has several new features with a unique mathematical model. It uses adaptive weights to simulate the process of producing positive and negative feedback of the propagation wave of slime mould. This is based on bio-oscillator to form the optimal path for connecting food with excellent exploratory ability and exploitation propensity.
- Stage 3: In the next stage, the CNN model is introduced as the first extraction layer of deep learning. The introduction of CNN helps in reducing dimensionality and thereby reduces the computation time. CNN entails a data processor including feature extractors drawing upon statistically significant antecedent lagged predictor variables.
- Stage 4: In the next stage, the model building employed four independent LSTMs to encapsulate feature mapping schemes.
- Stage 5: For further model building stage, another CNN layer was employed on the LSTM outputs. The convolutional layers in the second CNN model apply the convolution operation on time series data (input from LSTM) to extract spatial patterns and intrinsic characteristics from diverse meteorological variables. CNNs typically consist of several levels of convolutional-pooling layers and there are several convolutions runs are performed on each layer to collect useful information. The second layer boosts the efficacy and accuracy of resultant hybrid SCLC by extracting effective features, finding the interdependence of data in time series, and detecting the best mode suitable for relevant data. During this process, the CNN uses weights for the meteorological parameter based on its effect on *GSR*.

- Stage 6: Lastly, the final output from stage five goes through the fully connected (FC) layer (MLP) resulting in next-day *GSR* prediction. The proposed hybrid SMA-CNN-LSTM-CNN-MLP (SCLC) final layer has fully connected dense layers and can predict *GSR* over some time.

The CNN unit's output is a flattened feature vector $h^l = (h_1, h_2, \ldots, h_l)$ where l represents the number of filters in CNN. The Eq. (15) represents the equation deployed at that level. σ is a non-linear activation function, w is the weight of the ith node for layer $l-1$ and jth node for layer l, and b_i^{l-1} represent bias.

$$d_i^l = \sum_j w_{ji}^{l-1} \left(\sigma(h_i^{l-1}) + b_i^{l-1}\right) \tag{15}$$

The proposed hybrid SCLC model is depicted in Fig. 2. The first CNN layer is composed of four convolutional layers followed by a pooling layer, then the results are flattened. Convolutional layer 1 reads through input data (predictor) and displays results as feature maps, layer 2 and layer 3 perform the same operation on feature maps created by layer 1 and layer 2 respectively, and layer 4 repeats the process to amplify any salient features. Feature maps that are extracted after layer 4 are then flattened and fed to the 3-layer stacked LSTM model. The next step involves transferring the LSTM extracted temporal information from predictor variables to the input layer of the second CNN model (3 Convolutional layers and 3 pooling layers). The feature maps extracted after the pooling layer of the second CNN are then flattened into a long vector (1-dimensional array). Lastly, we use a fully connected layer (*i.e.*, dense) to aggregate the data and predict the *GSR* by analysing the extracted features. In this architecture, spatial and temporal features are extracted independently with CNNs and LSTMs, hence using the positive aspects of both CNNs and LSTMs and producing a robust model.

2.3.1. Data normalization

In the prediction task, numerical values with different scales must be normalized, ignoring this step hinders gradient descent-based algorithms, resulting in slower convergence speeds and distorting prediction results [99]. Thus, this study has utilized the Z-score normalization method to the predictor dataset intending to scale all the variables to a similar range. Let $X = \{x_1, x_2, \ldots, x_L\}$ be the considered time-series input data with L component. Each sample of X was normalized with a centre of 0 and a standard deviation of 1 by following Eq. (16):

$$\tilde{X} = \frac{x - \mu}{\sigma} \tag{16}$$

where μ and σ are the mean and standard deviation of X, respectively. Finally, the scaled data is represented with $\tilde{X} = \{\tilde{x}_1, \ldots, \tilde{x}_L\}$ and the subset of the input can be prepared. Since the normalization is invertible, the results are unaffected.

2.3.2. Feature selection

This study has utilized the meta-heuristic (SMA) as search algorithm and K-Nearest Neighbour Regressor (KNNR) as a machine learning algorithm for the selection of optimal input. SMA feature selection process involves the partitioning of the normative (*GSR*) data into training sets and testing sets (e.g., 80% for training, 20% for testing in 5-fold cross-validation) and running the KNNR on the selected features in the dataset. Each feature subset considered in the SMA FS is trained by the KNNR and its performance is evaluated by measuring the generalization performance on the original data. Feature subsets with minimum RMSE are considered the optimal subset. The SMA feature selection works on the below configuration:

- Total Population $(N) = [10, 20, 50, 80, 100, 200, 300, 500]$.
- Count of maximum iterations $(T) = 50$.
- Number of k in K-nearest neighbour $(K) = 5$
- Probability of exploration and exploitation capability $(z) = 0.03$

The performance of the RMSE (Fitness Value, FV) determines the population size that in turn affects the SMA feature selection performance. Hence, the study assessed the objective SMA FS with respect to the populations. The convergence curve was plotted to show the optimal fitness value in the slime mould during the iteration process. Based on the convergence curve (Fig. 7), it can be concluded that population increases are not always beneficial for FV, at Cape York solar storage when population size (N) was increased from 50 to 300, there was an only minimum change in the fitness value (with N = 50, FV = 2.05 and N = 300, FV = 1.98). Additionally, computationally inefficiency creeps in with the higher size so for the remaining solar farms, 300 is the limit of the population size. This balances the FV with the algorithm computation time. Thus for Barunggam, Cameby, and Chinchilla solar farms, 17 predictors are selected from 75 (predictor matrix: 20455 × 17). Whereas for Cape York and Sun metals solar farm only 12 predictors are chosen (predictor matrix: 20455 × 12), and Clermont gets 13 (predictor matrix: 20455 × 16). Table 3 shows the complete SMA feature selection process, along with predictor and predictands (*GSR*) matrix of correlation for Fig. 8.

2.3.3. Data partition

Finally, the SMA selected predictor matrix is merged with predictands (*GSR*) to get the input-target data for supervised machine learning. Before integrating all data are created to predict daily *GSR*. The models are calibrated on the training set while the validation set does not participate in training and helps to tune the models during the model development phase. The test set is only used after a model has been trained (using train and validation sets), mostly for model evaluation. This paper uses (20089 data points) or 54 years of training data. Of which 4018 data points or 20% of the data is used in validation and 365 data points or an year of data is sued for testing.

2.3.4. Benchmark model development

A comparison of the SCLC model with five popular forecast models, such as CNN-LSTM, Deep Neural Network (DNN), Artificial neural network (GBM), SADE-ELM, and Random Forest Regression (RFR), was done. The complete modelling was done in the Python using Keras 2.2.4 [100,77] on TensorFlow 1.13.1 [101,77]. 32 GB of RAM with®Core™ processor was used.

2.3.5. Model tuning

All the ML models have different hyperparameters that determine both the network structure (e.g., number of filters, neurons) and how the network models are trained (e.g., type of optimizer, activation function) [102]. As such, the performance of an ML model can vary greatly depending on its chosen set of hyperparameters therefore to achieve optimal performance hyperparameters should be selected cautiously [103]. The authors in this study used five-fold cross-validation method [104,105] for the grid-search of all the hyperparameters. Evaluation was based on its average RMSE on the validation set for each set of hyperparameters. In grid search, all possible combinations of hyperparameters are tried for a dataset to find the best hyperparameter. Furthermore, during deep learning model (SCLC and CLSTM) training, rectified linear unit (ReLu) activation function is used in all except the last layer. ReLu performs better than sigmoid and hyperbolic tangent activation functions and does not have the vanishing gradient problem [106]. Adam is an adaptive learning rate optimization algorithm designed to train neural networks [107]. The name Adam comes from adaptive moment estimation [108] and uses a quadratic gradient to change the learning rate, as well as the momentum based on the moving average of the gradient. Furthermore, this study also employed the following regularization technique when developing a robust deep learning model for *GSR* prediction.

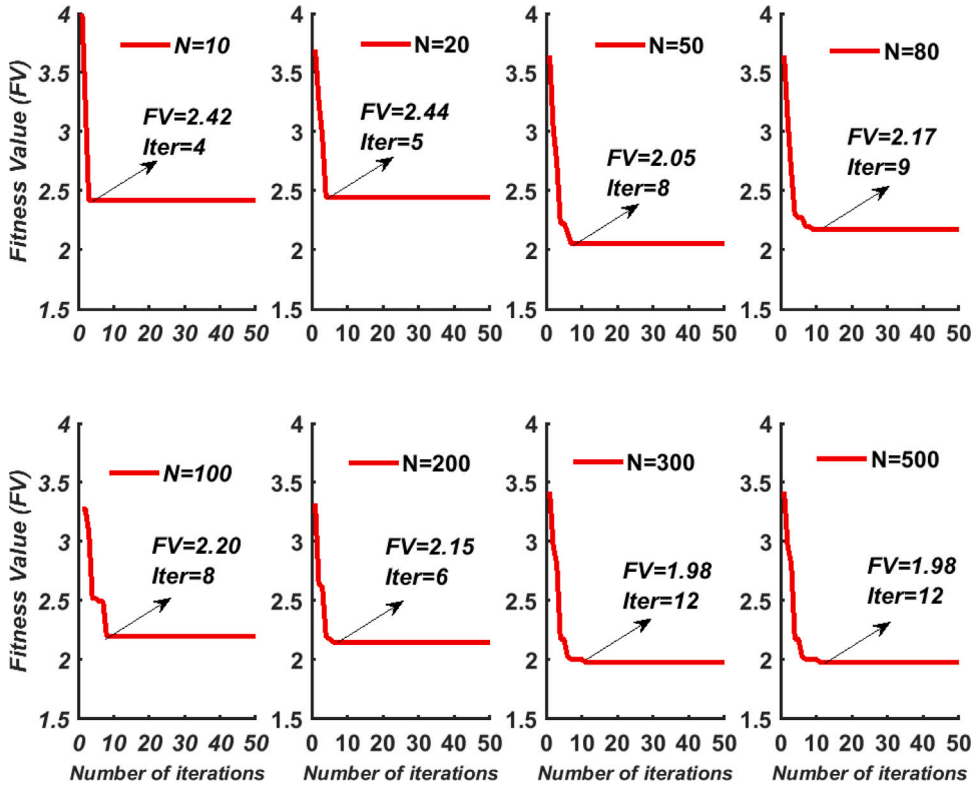

Fig. 7. Convergence curve for SMA feature selection on predictors of Cape York solar storage.

Table 3
Chosen Input predictor variable for all farms through Slime Mould Optimization feature selection. Table 2 shows the abbreviations.

Barunggam	Cameby	Cape York Solar Storage	Chinchilla	Clermont	Sun Metals
Evap	Evap	Evap	Evap	Evap	Evap
RHmaxT	RHmaxT	RHmaxT	RHmaxT	RHmaxT	RHmaxT
ua_1000	ua_1000	hfss	ua_1000	hfss	hfss
hfls	hfls	hur_1000	hfls	hur_1000	Rain
hfss	hfss	Rain	hus_5000	T.Max	hur_1000
hus_5000	hus_5000	T.Max	hfss	Rain	hfls
wap_1000	ta_25000	hur_85000	wap_1000	ua_5000	T.Max
ta_25000	wap_1000	hus_1000	ta_25000	wap_1000	ua_5000
wap_85000	sfcWindmax	wap_1000	sfcWindmax	va_85000	va_50000
zg_1000	zg_1000	va_70000	zg_1000	RHminT	zg_5000
sfcWindmax	Rain	uas	wap_85000	wap_85000	wap_1000
ua_5000	RHminT	RHminT	Rain	zg_5000	hur_70000
RHminT	wap_85000		RHminT	va_50000	ta_25000
Rain	ua_10000		ua_5000	hfls	
T.Max	hur_1000		hur_1000	sfcWindmax	
va_25000	psl		va_25000	hus_5000	
hur_1000	va_25000		T.Max		

- During training, the dropout technique was employed to prevent overfitting and enhance performance. The dropout involves dumping a certain number of neurons randomly on the network. The connections of the dropped neurons, therefore, are ignored [109].
- ReduceLROnPlateau regularization was employed to monitor the improvement of validation loss (root mean square error; RMSE), and in the case that no improvement is verified for a 'patience' number of 10 iterations, the learning rate (lr) is reduced at the factor of 0.2($lr_{new} = lr \times 0.2$). Consequently, when the learning process stagnates, this reducing strategy could be of significant benefit to the model [110,111].
- The early stopping (es) regularization method monitors the loss of the validation set and stop stops the training when the validation loss is no longer decreasing for a certain number of epochs [112]. Hence, with es the training can be stopped when no further important improvements can be achieved or when the validation loss starts to increase due to overfitting [113]. In this study, the training was stopped after the loss stopped decreasing for 15 consecutive epochs.

It should be also noted that in this study the es and ReduceLROnPlateau were not used along with grid search because the programming code did not permit to integrate them. Therefore, these regularization methods were only used during the training of the final model with optimal parameters. Tables 4 and 5 list the search space and optimized results for the hybrid SCLC as well as other benchmark models. Fig. 9 shows the losses of the proposed SCLC model (Cape York solar storage). There is a slow decrease of both losses showing good SCLC model performance.

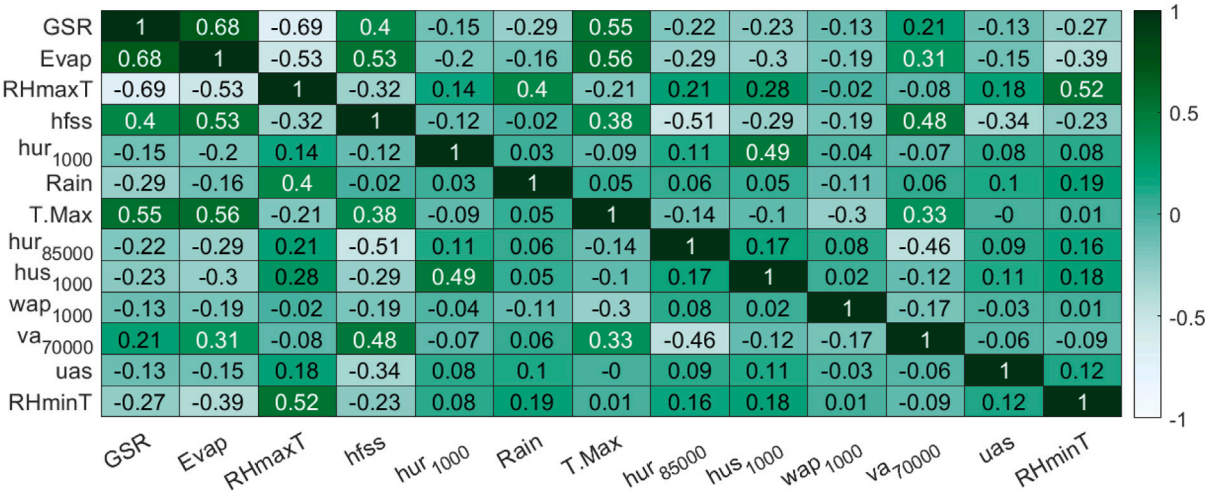

Fig. 8. A Correlation matrix for Cape York solar storage. Note: -Table 2 outlines the nomenclature.

Table 4
(a) The objective deep learning hybrid model (SCLC) with other deep learning models (i.e., Convolution Neural Network integrated with Long-term short-term Memory), CLSTM, and Network Deep Neural Network (DNN).

Predictive deep learning models	Model hyperparameters	Hyperparameter selection	Barunggam Solar Farm	Cameby Solar Farm	Cape York Solar Storage	Chinchilla Solar Farm	Clermont Solar Farm	Sun metals Solar Farm
SCLC	Filter1 (for first CNN)	[50, 80, 100, 200]	100	200	50	80	50	100
	Filter 2 (for first CNN)	[40, 50, 60, 70, 80]	70	40	50	80	40	60
	Filter 3 (for first CNN)	[20, 10, 30, 5]	30	30	20	30	30	30
	LSTM cell 1	[100]						
	Drop rate	[0, 0.1, 0.2]	0	0.1	0	0.2	0.1	0
	LSTM cell 2	[80]						
	LSTM cell 3	[50]						
	Filter1 (for second CNN)	[50, 80, 100, 200]	80	50	50	80	200	50
	Filter 2 (for second CNN)	[40, 50, 60, 70, 80]	70	40	60	60	80	40
	Filter 3 (for second CNN)	[20, 10, 30, 5]	20	30	30	30	20	10
	Epochs	[300, 400, 500, 600, 700]	500	400	600	700	500	400
	Batch size	[5, 10, 15, 20, 25, 30]	10	15	5	20	25	5
CLSTM	Filter1	[50, 80, 100, 200]	80	50	100	100	80	80
	Filter 2	[40, 50, 60, 70, 80]	40	60	50	60	80	70
	Filter 3	[20, 10, 30, 5]	10	5	30	10	20	30
	LSTM cell 1	[50, 60, 100, 200]	50	60	100	60	50	100
	LSTM cell 2	[40, 50, 60, 70, 130]	40	50	70	40	50	40
	LSTM cell 3	[20, 10, 30, 5]	20	10	10	30	20	10
	LSTM cell 4, 5 and 6	[Fixed as 30, 20, 10]						
	Activation function	ReLu						
	Epochs	[300, 400, 500, 600, 700]	500	400	300	600	300	400
	Drop rate	[0, 0.1, 0.2]	0.1	0	0	0.1	0	0
	Batch size	[5, 10, 15, 20, 25, 30]	5	10	5	15	25	10
DNN	Hidden neuron 1	[100, 200, 300, 400, 50]	100	200	50	80	50	100
	Hidden neuron 2	[20, 30, 40, 50, 60, 70]	70	40	50	80	40	60
	Hidden neuron 3	[10, 20, 30, 40, 50]	30	30	20	30	30	30
	Hidden neuron 4	[5, 6,7, 8,12, 15, 18]	12	15	15	12	5	8
	Activation function	ReLu						
	Epochs	[300, 400, 500, 600, 700]	400	400	600	500	700	300
	Drop rate	0.1						
	Batch size	[5, 10, 15, 20, 25, 30]	15	20	25	5	10	10

2.3.6. *Performance evaluation metrics*

Statistical metrics based on earlier approaches [35,38,45,114–120] were employed to assess the performance of the hybrid CXGBRFR model.

$$r = \frac{\sum_{i=1}^{n}(GSR^m - \langle GSR^m\rangle)(GSR^p - \langle GSR^p\rangle)}{\sqrt{\sum_{i=1}^{n}(GSR^m - \langle GSR^m\rangle)^2}\sqrt{\sum_{i=1}^{n}(GSR^p - \langle GSR^p\rangle)^2}} \quad (17)$$

$$RMSE = \sqrt{\frac{1}{n}\sum_{i=1}^{n}(GSR^p - GSR^m)^2} \quad (18)$$

$$MAE = \frac{1}{n}\sum_{i=1}^{n}|GSR^p - GSR^m| \quad (19)$$

$$RRMSE = \frac{\sqrt{\frac{1}{n}\sum_{i=1}^{n}(GSR^p - GSR^m)^2}}{\langle GSR^m\rangle} \quad (20)$$

$$RMAE = \frac{1}{n}\sum_{i=1}^{n}\frac{|GSR^p - GSR^m|}{GSR^p} \quad (21)$$

$$WI = 1 - \frac{\sum_{i=n}^{n}(GSR^m - GSR^p)^2}{\sum_{i=n}^{n}(|GSR^p - \langle GSR^m\rangle| + |GSR^m - \langle GSR^m\rangle|)^2} \quad (22)$$

$$NSE = 1 - \frac{\sum_{i=1}^{n}(GSR^m - GSR^p)^2}{\sum_{i=1}^{n}(GSR^m - \langle GSR^m\rangle)^2} \quad (23)$$

$$LM = 1 - \frac{\sum_{i=1}^{n}|GSR^m - GSR^p|}{\sum_{i=1}^{n}|GSR^m - \langle GSR^m\rangle|} \quad (24)$$

Table 5
(b) Comparison of machine learning models used in the study. Note that ReLU is Rectified Linear Units. Tansig, logsig and purelin refer to Hyperbolic tangent transfer function, Log-sigmoid transfer function, and linear transfer function respectively. LM, lbfgs, cgf, rp, br, scg refer to Levenberg–Marquardt, limited memory Broyden–Fletcher–Goldfarb–Shanno, Conjugate gradient backpropagation with Fletcher–Reeves, resilient backpropagation, Bayesian regulation backpropagation, and one-step secant backpropagation algorithm respectively.

Predictive conventional models	Model hyperparameters	Hyperparameter selection	Barunggam Solar Farm	Cameby Solar Farm	Cape York Solar Storage	Chinchilla Solar Farm	Clermont Solar Farm	Sun Metals Solar Farm
ANN	Hidden neuron	[10, 20, 30, 40, 60, 80, 100, 200, 300]	200	100	60	80	100	200
	Training Function	['trainlm', trainbfg, traingdx]	trainlm	trainlm	trainbfg	trainbfg	trainbfg	trainlm
	Activation function	[tansig, logsig, purlin]	tansig	tansig	logsig	logsig	logsig	tansig
SADE-ELM	Hidden neuron	[20, 40, 80, 100]	80	100	80	40	80	100
	Activation function	[sig]						
	Crossover ratio	0.5						
	Population	100						
	Amplification factor	0.5						
	Maximum Generation	100						
RFR	The maximum depth of the tree.	[5, 8, 10, 20, 25]	10	20	10	10	25	10
	The number of trees in the forest.	[50, 100, 150, 200]	100	150	50	150	100	150
	Minimum number of samples to split an internal node	[2, 4, 6, 8, 10]	8	8	6	10	6	8
	The number of features to consider when looking for the best split.	['auto', 'sqrt', 'log2']	auto	auto	auto	auto	auto	auto

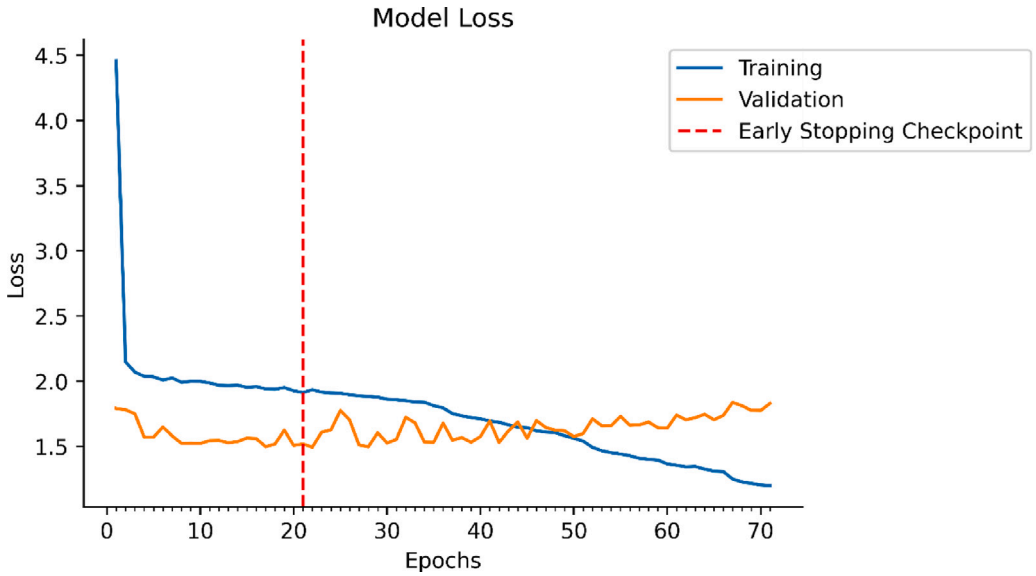

Fig. 9. Losses (training and validation with mean absolute error) for the prediction of *GSR*. Absence of loss improvement with predefined epochs calls for the early stopping callbacks.

$$E_{var} = 1 - \frac{\mathrm{Var}(GSR^m - GSR^p)}{\mathrm{Var}(GSR^m)} \tag{25}$$

$$SS = 1 - \frac{RMSE(p,x)}{RMSE(pr,x)} \tag{26}$$

$$RMSE_r = \frac{RMSE(p,x)}{RMSE(r,x)} \tag{27}$$

where GSR^p and GSR^m denote *GSR*'s predicted and observed value, $\langle GSR^m \rangle$ s well as $\langle GSR^p \rangle$ denote observed as well as predicted *GSR* mean, prediction of model is shown via p, observation is x, perfect prediction (persistence) is pr, and prediction of reference is r.

To improve the performance of model,

- r varies from −1 and +1, MAE, RMSE values go from 0 (best fit) to ∞ that show the fit that is worst);
- RRMSE and RMAE can be in the range (0%–100%) [121].
- Willmot Index is better metrics. It varies from the values of the worst fit of 0 to perfect fit of 1 [122].
- NSE, keeps a tab on the variance of *GSR* with the worst fit as −∞ and 1 being the perfect fit [123].
- Legates shows to be best of all with preferred values between 0–1 [124].
- E_{var}; takes care of the biased variance.

Global Performance Indicator (GPI) is used to rank the overall model performance [125]

$$\mathrm{GPI}_i = \sum_{j=1}^{6} \alpha_j (g_j - y_{ij}) \tag{28}$$

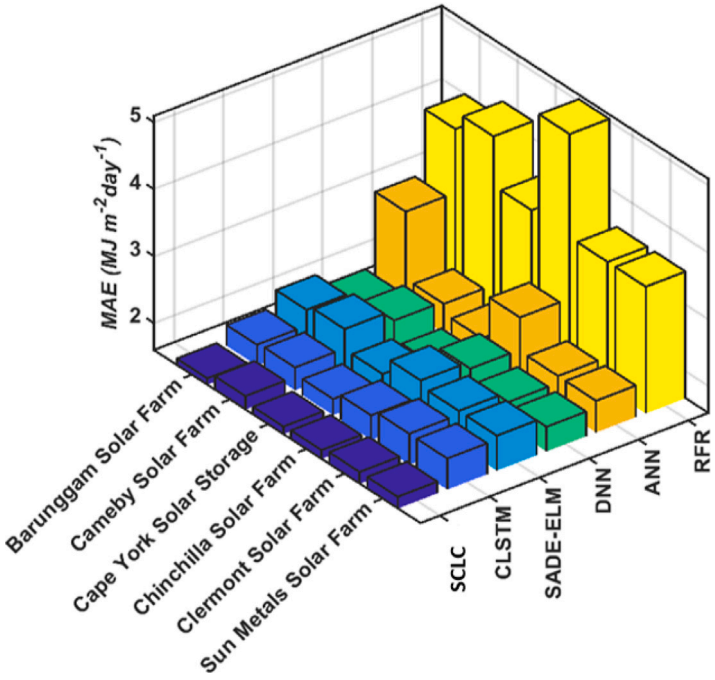

Fig. 10. Evaluation of Deep hybrid model SCLC and its comparative approaches in the testing phase, through mean absolute error (MAE, MJm^{-2} day^{-1}). (Note: Nomenclature of every model is in Tables 3–5).

where α_j denotes the median of scaled values of statistical indicator j. Higher value shows the better performance. There is also the use of the Kling–Gupta Efficiency (KGE) [126] and Absolute Percentage Bias (APB; %) [127]. We shows these mathematically as follows:

$$KGE = 1 - \sqrt{(r-1)^2 + \left(\frac{\langle GSR^p \rangle}{\langle GSR^m \rangle} - 1\right)^2 + \left(\frac{CV_p}{CV_m}\right)^2} \tag{29}$$

$$APB = \frac{\sum_{i=1}^{n}((GSR^m - GSR^p) * 100)}{\sum_{i=1}^{n} GSR^m}, \tag{30}$$

where r is the correlation coefficient, CV is the coefficient of variation, GSR^p refers to the predicted GSR ($MJm^{-2}day^{-1}$), GSR^m is the measured GSR^p ($MJm^{-2}day^{-1}$), $\langle GSR^m \rangle$ is the average value of the GSR^m, $\langle GSR^p \rangle$ shows the average value of the GSR^p. Actual values are shown by n.

Furthermore, the following metrics are also used: Mean Absolute Error (λ_{MAE}), Absolute Percentage Bias (λ_{APB}), and Root Mean Square Error (λ_{RMSE}) [128].

$$\lambda_{APB} = \left|\frac{APB_1 - APB_2}{APB_1}\right| \tag{31}$$

$$\lambda_{MAE} = \left|\frac{RMAE_1 - RMAE_2}{RMAE_1}\right| \tag{32}$$

$$\lambda_{RRMSE} = \left|\frac{RRMSE_1 - RRMSE_2}{RRMSE_1}\right| \tag{33}$$

where, APB_1, $RRMSE_1$ and $RMAE_1$ show the performance of (*i.e.*, SCLC) and competitiveness is shown via $RRMSE_2$, APB_2, and $RMAE_2$ refers to the benchmark model performance metrics.

Directional Symmetry (DS) calculates the performance as below:

$$DS = \frac{1}{n}\sum_{t=2}^{n} d_t \times 100\% \tag{34}$$

where

$$d_t = \begin{cases} 1, & \text{if}(GSR_t^m - GSR_{t-1}^m)(GSR_t^p - GSR_{t-1}^m) > 0 \\ 0, & \text{otherwise} \end{cases} \tag{35}$$

Another performance metrics used for statistical significance are the Harvey, the Newbold (HLN), Diebold–Mariano (DM) test, and Leybourne. The main steps are stated in the published literature [114–116].

3. Results and discussion

The deep hybrid SCLC model used for GSR prediction was able to produce a high r-value and lower MAE and RMSE values for the Barunggam Solar Farm ($r \approx 0.930$, RMSE $\approx$ 2.338 $MJm^{-2}day^{-1}$, MAE $\approx$ 1.69 $MJm^{-2}day^{-1}$). This contrasted the results of the deep learning model CNN-LSTM model ($r \approx 0.916$, RMSE $\approx$ 2.538 $MJm^{-2}day^{-1}$, MAE $\approx$ 1.911 $MJm^{-2}day^{-1}$) and the DNN model ($r \approx 0.914$, RMSE $\approx$ 2.633 $MJm^{-2}day^{-1}$, MAE $\approx$ 1.946 $MJm^{-2}day^{-1}$). Likewise, for the conventional ML models (ANN, SADE-ELM, and RFR) the r-value is lower than that of the SCLC model, RMSE, and MAE, both metrics are higher than that of the SCLC model. Additionally, for remaining solar farms, the SCLC produced substantially healthier *GSR* prediction (Table 6 and Fig. 10). This result shows that the SCLC is a possible choice to be implemented as a well-designed forecasting approach for *GSR* predictions in comparison to DL-based models (CLSTM and DNN), and traditional ML models.

In Table 7, to compare the SCLC model against CLSTM, DNN, ANN, SADE-ELM, and RFR models, we utilized multiple criteria based on WI and NSE. According to these model penalization metrics, the results produced by the SCLC model for the case of Barunggam Solar Farm yielded a value of (WI $\approx$ 0.926, NSE $\approx$ 0.862), CLSTM (WI $\approx$ 0.913, NSE $\approx$ 0.8377), DNN (WI $\approx$ 0.904, NSE $\approx$ 0.826), ANN (NSE $\approx$ 0.6331, WI $\approx$ 0.723), SADE-ELM model (WI $\approx$ 0.886, NSE $\approx$ 0.795) and RFR model (WI $\approx$ 0.564, NSE $\approx$ 0.390). Remaining model penalization metrics like LM and Evar (Table 8) were also utilized and for the solar farm of Barunggam, the SCLC with better Legates and Evar (LM $\approx$ 0.674, Evar $\approx$ 0.864) outperform all other DL models as well as the benchmark ML models. Furthermore, SCLC model of remaining solar farms (Cameby, Cape York Solar Storage, Chinchilla, Clermont, and Sun Metals Solar Farm) performed nicely. Compared to r, RMSE, and MAE, these higher-order metrics demonstrate that the SCLC has better predictive abilities to deliver accurate prediction of *GSR*.

Table 6
SCLC model vs. other comparative models in the testing phase for all the solar farms considered in the study measured with respect to the correlation coefficient (r) and root mean square error ($RMSE$, $MJm^{-2}day^{-1}$) in the model's testing phase. The Objective model SCLC is blue bold-faced.

Predictive models	Barunggam Solar Farm		Cameby Solar Farm		Cape York Solar Storage		Chinchilla Solar Farm		Clermont Solar Farm		Sun Metals Solar Farm	
	r	$RMSE$	r	$RMSE$	r	$RMSE$	r	$RMSE$	r	$RMSE$	r	$RMSE$
SCLC	**0.930**	**2.338**	**0.930**	**2.386**	**0.880**	**2.207**	**0.933**	**2.314**	**0.905**	**2.502**	**0.935**	**2.792**
CLSTM	0.916	2.538	0.910	2.653	0.863	2.441	0.910	2.638	0.881	2.761	0.920	3.091
SADE-ELM	0.895	2.849	0.895	2.911	0.853	2.539	0.893	2.833	0.878	2.793	0.920	3.106
DNN	0.914	2.633	0.901	2.772	0.881	2.384	0.898	2.787	0.891	2.647	0.895	3.389
ANN	0.899	3.815	0.910	2.705	0.864	2.507	0.833	3.471	0.881	2.778	0.892	3.627
RFR	0.681	5.033	0.694	5.492	0.578	4.515	0.516	6.135	0.686	4.574	0.839	4.462

Table 7
SCLC model vs. other comparative models in the testing phase for all the solar farms considered in the study measured with respect to the Willmott's Index (WI) and Nash–Sutcliffe coefficients (NSE).

Predictive models	Barunggam Solar Farm		Cameby Solar Farm		Cape York Solar Storage		Chinchilla Solar Farm		Clermont Solar Farm		Sun Metals Solar Farm	
	WI	NSE	WI	NSE	WI	NSE	WI	NSE	WI	NSE	WI	NSE
SCLC	**0.926**	**0.862**	**0.922**	**0.858**	**0.873**	**0.769**	**0.928**	**0.865**	**0.906**	**0.816**	**0.874**	**0.756**
CLSTM	0.913	0.837	0.900	0.822	0.830	0.724	0.903	0.824	0.886	0.775	0.820	0.703
SADE-ELM	0.886	0.795	0.888	0.788	0.808	0.704	0.891	0.796	0.888	0.770	0.814	0.701
DNN	0.904	0.826	0.897	0.807	0.829	0.741	0.896	0.803	0.900	0.793	0.808	0.640
ANN	0.723	0.631	0.896	0.818	0.795	0.710	0.821	0.694	0.883	0.772	0.700	0.592
RFR	0.564	0.390	0.690	0.245	0.443	0.134	0.438	0.062	0.606	0.407	0.727	0.376

Table 8
SCLC model vs. other comparative models in the testing phase for all the solar farms considered in the study measured with respect to the Legates and McCabes index (LM) and explained variance score (E_{var}).

Predictive models	Barunggam Solar Farm		Cameby Solar Farm		Cape York Solar Storage		Chinchilla Solar Farm		Clermont Solar Farm		Sun Metals Solar Farm	
	LM	E_{var}	LM	E_{var}	LM	E_{var}	LM	E_{var}	LM	E_{var}	LM	E_{var}
SCLC	**0.674**	**0.864**	**0.653**	**0.865**	**0.539**	**0.772**	**0.665**	**0.870**	**0.623**	**0.819**	**0.525**	**0.757**
CLSTM	0.632	0.839	0.626	0.822	0.505	0.744	0.620	0.828	0.562	0.776	0.491	0.710
SADE-ELM	0.586	0.800	0.570	0.796	0.481	0.728	0.574	0.798	0.549	0.771	0.490	0.707
DNN	0.625	0.836	0.600	0.811	0.515	0.774	0.595	0.807	0.582	0.793	0.444	0.641
ANN	0.413	0.631	0.607	0.828	0.490	0.733	0.502	0.694	0.559	0.774	0.389	0.599
RFR	0.230	0.411	0.179	0.246	0.052	0.150	0.027	0.064	0.258	0.424	0.223	0.376

Table 9
SCLC model vs. other comparative models in the testing phase for all the solar farms considered in the study measured with respect to the relative mean absolute error ($RMAE$, %) and relative root mean square error ($RRMSE$, %)

Predictive models	Barunggam		Cameby		Cape York Solar Storage		Chinchilla		Clermont		Sun Metals	
	$RRMSE$	$RMAE$	$RRMSE$	$RMAE$	$RRMSE$	$RMAE$	$RRMSE$	$RMAE$	$RRMSE$	$RMAE$	$RRMSE$	$RMAE$
SCLC	**11.66%**	**10.71%**	**11.84%**	**11.12%**	**11.46%**	**10.37%**	**11.56%**	**10.61%**	**12.17%**	**10.85%**	**13.67%**	**13.12%**
CLSTM	12.65%	12.28%	13.17%	12.68%	12.67%	11.61%	13.17%	12.34%	13.43%	12.54%	15.13%	14.96%
SADE-ELM	14.20%	13.75%	14.45%	13.59%	13.18%	12.23%	14.15%	13.61%	13.59%	12.92%	15.20%	15.41%
DNN	13.13%	12.15%	13.76%	12.49%	12.37%	11.52%	13.92%	12.55%	12.88%	11.58%	16.59%	16.11%
ANN	19.02%	20.09%	13.43%	13.18%	13.01%	12.41%	17.33%	16.77%	13.52%	12.58%	17.75%	19.10%
RFR	25.09%	26.83%	27.27%	26.86%	23.44%	21.53%	30.63%	32.18%	22.25%	23.10%	21.84%	21.40%

Overcoming the problem of the limitation of objective metrics in *GSR* prediction, the study uses for enhancing the proposed model's suitability. Fig. 10 illustrates the scatterplots in the testing phase for the observed and predicted *GSR* With scatter points being closer to the $y = mx + C$ the proposed SCLC performs the best. Results matches with the results of all other metrics.

RRMSE and RMAE compares the performance of models where the stations differ physically, geographically, and climatically. (Table 9) showed that proposed model carries minimum RRMSE and RMAE than CLSTM, DNN, ANN, SADE-ELM & RFR for all the study sites. SCLC model at Cape York Solar Storage produces the lowest (RRMSE ≈ 11.46%, RMAE≈ 10.37%) relative metrics in comparison to others. All calculations indicate the best ability of SCLC model.

The SCLC model is compared by Promoting Percentages via (λ) for instance, λ = RMAECLC-RMAECLSTM, is evaluated to estimate the difference in the relative mean absolute error of SCLC and CLSTM model. Table 10 compares the SCLC model with the other models tested during the testing phase. SCLC outperforms CLSTM and others.

Graphically analysing carries a lot of importance as being numerical evaluation of the model. Fig. 12 shows the boxplots of the SCLC with comparative approaches. Figure shows, the + symbols represent the outliers of the extreme absolute prediction error ($|PE| = GSR_{obs-} - GSRpred$) of the testing data. Additionally, the kernel density estimate (KDE) plots of the standardized residuals were also plotted in Fig. 13 to get a clearer picture of the residual distributions. The KDE plot of the standardized residuals for the SCLC model is close to the standard normal. We have not performed any correlation tests, but with such a large sample size, a hypothesis of correlated residuals is unlikely to be rejected. Hence, the box plot (Fig. 10) and KDE plot of standardized residuals (Fig. 11) further confirm SCLC's superior accuracy in *GSR* prediction compared to other competing models.

To broadly gauge the efficiency, a comprehensive and unbiased assessment of models is carried out by plotting a Taylor graph [117]. Fig. 14 illustrates the statistical association between predicted and actual *GSR* based on r and standard deviation. By comparing r to standard deviation, it is shown that RFR, ANN, and SADE-ELM are not proper as their r to standard deviation was extremely far from the observed *GSR*, whereas deep learning model DNN and CLSTM overlap and are closer to observation. The SCLC model closely matched the actual *GSR* approving the prediction was better. To provide further

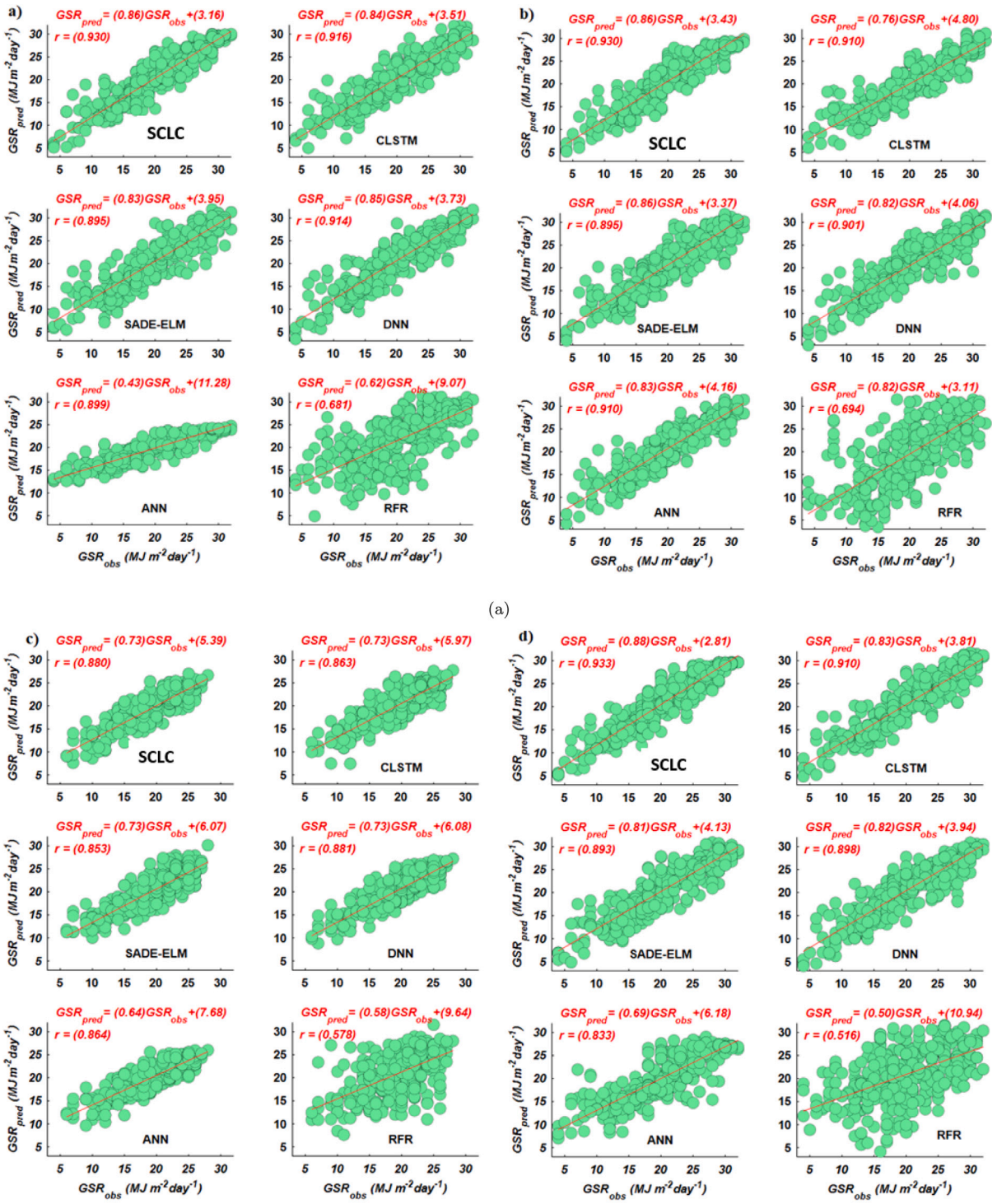

Fig. 11. Scatter plots of predicted (GSRpred) and observed (GSRobs) for all tested regions in Six solar farms of Queensland. (a) Barunggam, (b) Cameby Solar Farm, (c) Cape York Solar Storage, (d) Chinchilla, (e) Clermont and (f) Sun Metals. (Note: Red line is the least-squares fit line ($y = mx + c$. Table 3 as well as Tables 4 and 5) show the model nomenclature.

insight into the prediction capability of the proposed modelling systems for *GSR* prediction, Fig. 15 shows the plot for KGE, APB, and GPI. With high KGE (≈ 0.888) and low APB (≈ 9.035), the performance of the deep hybrid SCLC model far exceeds that of the counterpart models. Furthermore, the ranking of models is done according to their prediction efficiency using the GPI metrics. The GPI varies from −7.172 to 1.199 (Fig. 15(b)). The highest value of GPI of 1.199 is for SCLC, further cementing the advanced modelling capabilities of the proposed SCLC.

Additionally, statistical test DM, HLN, and DS were used to validate whether the prediction of SCLC having more accuracy as compared to the other comparative models. Tables 11 and 12 below show the statistics of the DM and HLN test results for all models. The models in the column of the table are compared with the model in the rows,

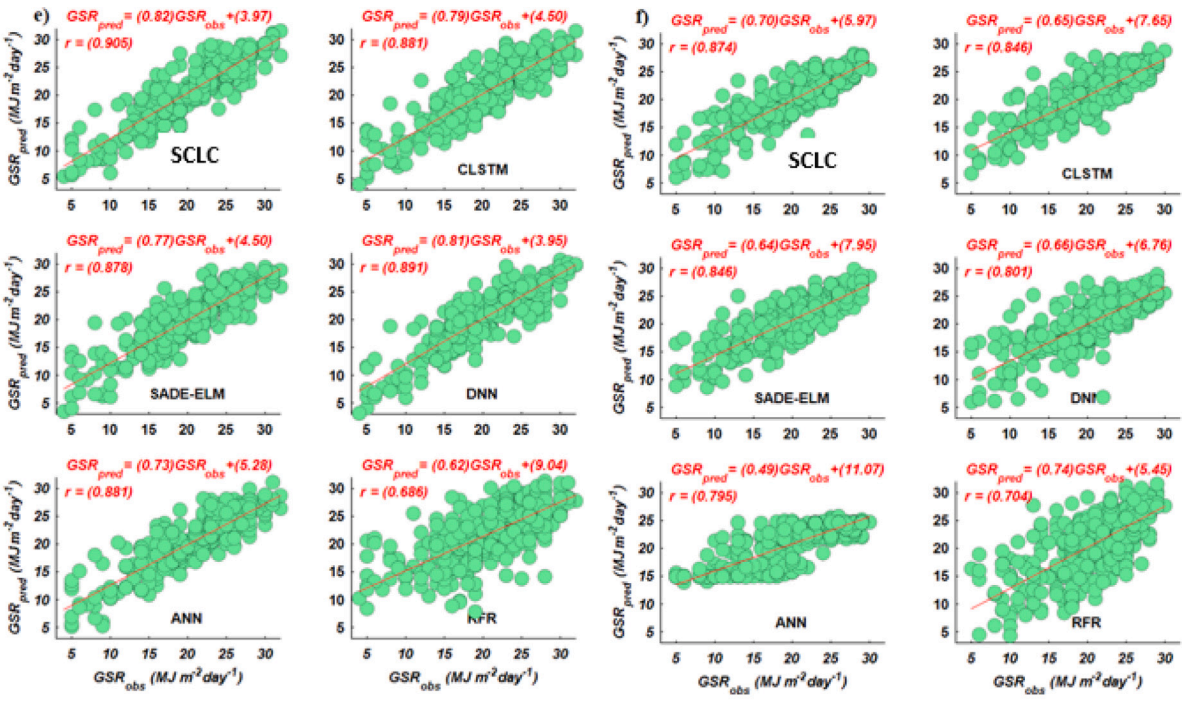

(c)

Fig. 11. (*continued*).

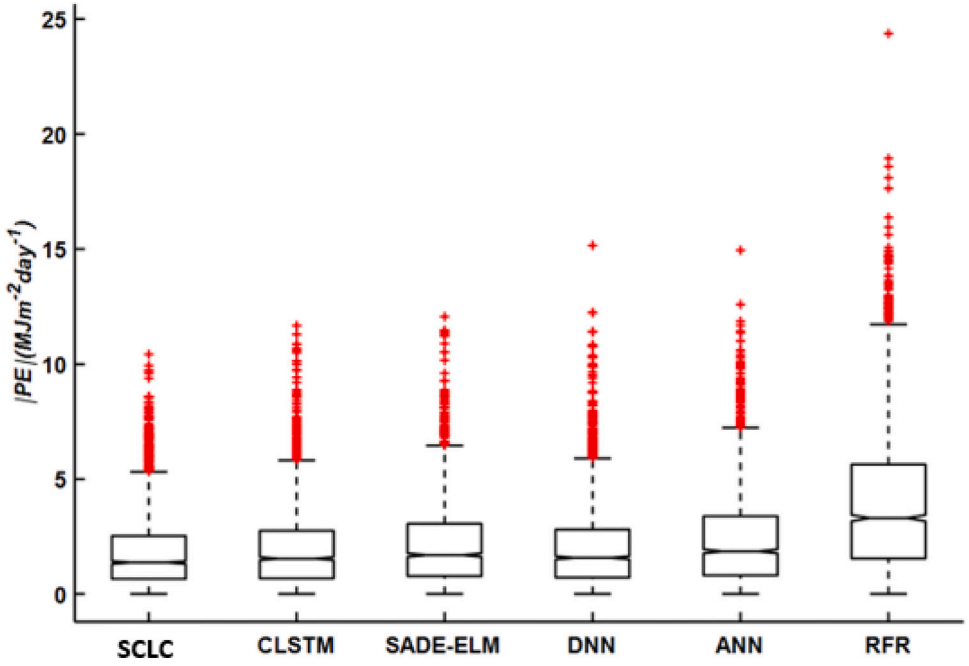

Fig. 12. Box plots of the prediction error (PE) generated by prediction models for prediction of *GSR*. (Note: Table 3 as well as Tables 4 and 5) show the nomenclatures.

Table 10
SCLC comparison of promoting percentage vs. the competitive models where the percentage shows the betterment of SCLC against the competitive models.

Predictive models	Barunggam Solar Farm			Cameby Solar Farm			Cape York Solar Storage			Chinchilla Solar Farm			Clermont Solar Farm			Sun Metals Solar Farm		
	λ_{RRMSE}	λ_{RMAE}	λ_{APB}	λ_{RRMSE}	λ_{RMAE}	λ_{APB}	λ_{RRMSE}	λ_{RMAE}	λ_{APB}	λ_{RRMSE}	λ_{RMAE}	λ_{APB}	λ_{RRMSE}	λ_{RMAE}	λ_{APB}	λ_{RRMSE}	λ_{RMAE}	λ_{APB}
CLSTM	9%	15%	13%	11%	14%	8%	11%	12%	7%	14%	16%	14%	10%	16%	16%	11%	14%	7%
SADE-ELM	22%	28%	27%	22%	22%	24%	15%	18%	13%	22%	28%	27%	12%	19%	19%	11%	17%	7%
DNN	13%	13%	15%	16%	12%	15%	8%	11%	5%	20%	18%	21%	6%	7%	11%	21%	23%	17%
ANN	63%	88%	80%	13%	18%	13%	14%	20%	11%	50%	58%	49%	11%	16%	17%	30%	46%	29%
RFR	115%	151%	136%	130%	141%	137%	105%	108%	106%	165%	203%	191%	83%	113%	97%	60%	63%	64%

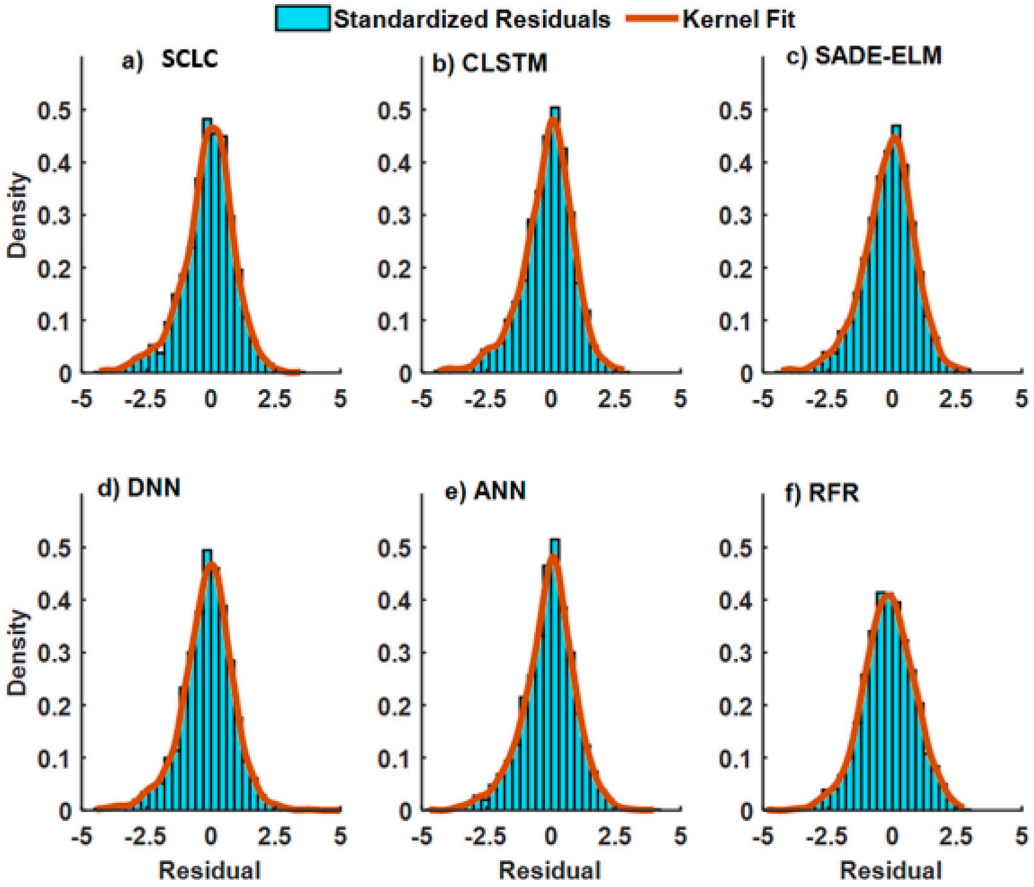

Fig. 13. Marginal kernel density estimate for the standardized residuals of the model, along with a standard normal density in red.

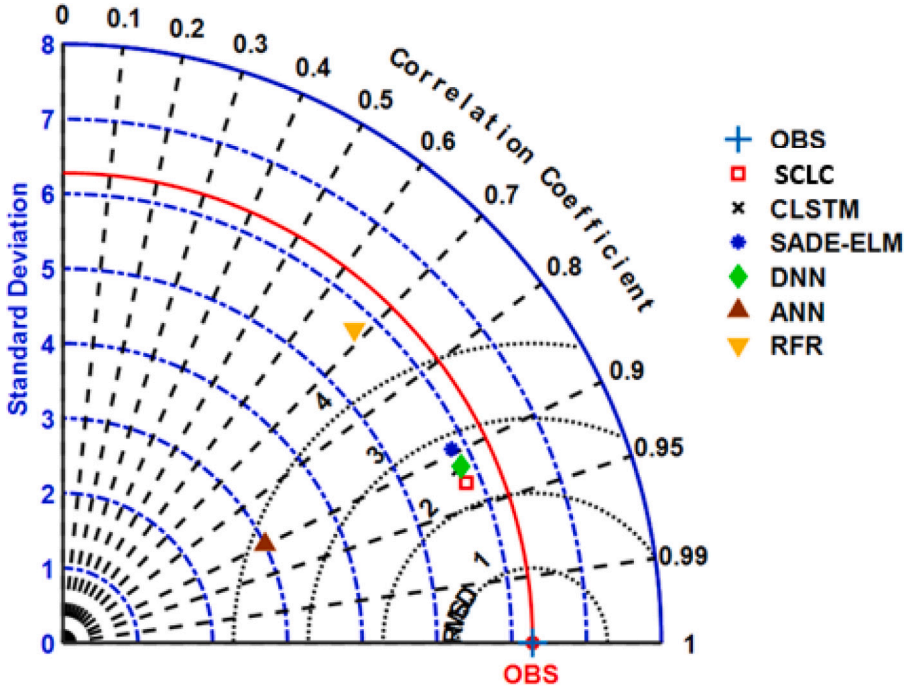

Fig. 14. Taylor plot for *GSR* prediction models.

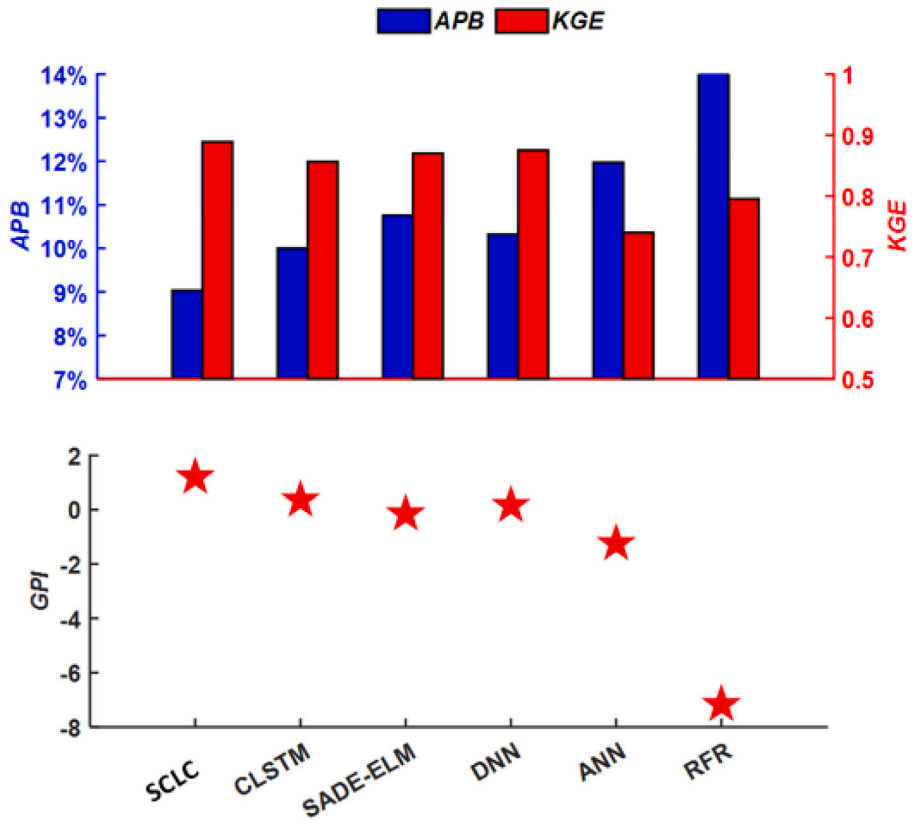

Fig. 15. (a) Bar chart showing a comparison of the SCLC model in the testing phases for Kling–Gupta efficiency and absolute percentage bias (APB, %). (b) SCLC model's Global performance indicator (GPI) with rest of artificial intelligence-based models. (Note: Model nomenclature are provided in Tables 3–5).

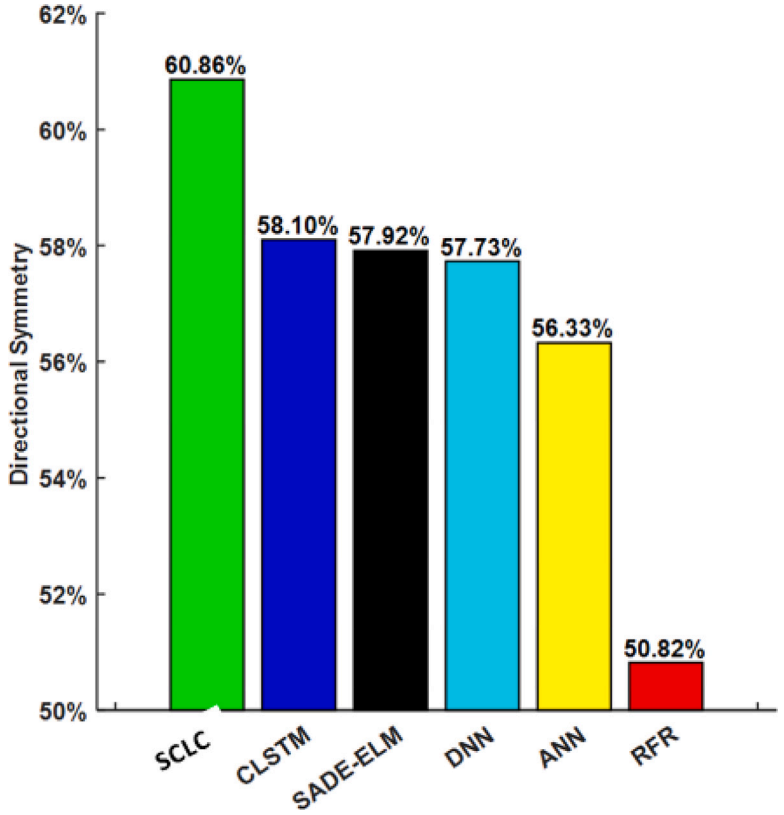

Fig. 16. Comparison of performance based on the Directional symmetry (DS) criteria of deep hybrid SCLC model with others. (Note: Model nomenclature shown in Table 3 as well as Tables 4 and 5).

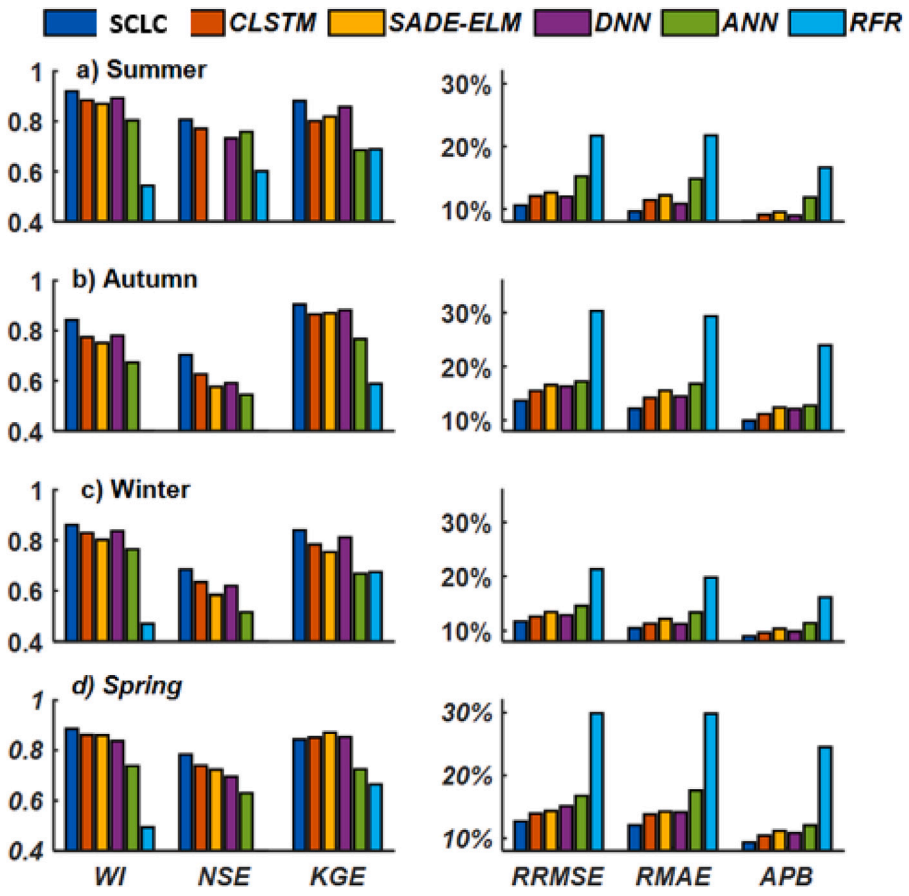

Fig. 17. Performance check of deep hybrid SCLC with others (Seasonal). The metrics used are Kling Gupta efficiency (KGE), Willmott's Index (WI), absolute percentage bias (APB, %), relative root mean square error (RRMSE, %), Nash–Sutcliffe Coefficient (NSE), and Relative mean absolute error (RMAE, %) (a) Summer, (b) Autumn, (c) Winter, and (d) Spring. (Note: Model nomenclature are provided in Tables 3–5).

Table 11
Statistics of the Diebold–Mariano (DM) test.(The column of the table is compared with the rows, and if the result is positive, the model in the column outperforms the one in the row; on the contrary, if it is negative, then the one in the row is superior).

Predictive models	SCLC	CLSTM	SADE-ELM	DNN	ANN	RFR
SCLC		**3.070**	**2.971**	**3.726**	**3.897**	**7.002**
CLSTM			0.225	1.691	2.910	5.545
SADE-ELM				1.728	2.993	5.694
DNN					1.249	4.646
ANN						2.993

Table 12
Statistics of Harvey, Leybourne, and Newbold test.

Predictive models	SCLC	CLSTM	SADE-ELM	DNN	ANN	RFR
SCLC		**3.216**	**3.112**	**3.903**	**4.083**	**7.335**
CLSTM			0.236	1.771	3.048	5.809
SADE-ELM				1.810	3.136	5.965
DNN					1.308	4.867
ANN						3.135

and if the result is positive, the model in the column outperforms the one in the row; on the contrary, if it is negative, then the one in the row is superior. Similarly, Fig. 16 shows that deep hybrid SCLC model DS (*i.e.*, directional prediction accuracy) is more than others, with an average of 60.86%. Congruency with earlier findings, DM, HLN, and DS test provides consistent results, which indicate that deep hybrid SCLC predicts *GSR* more accurately than other models.

Moreover, the RMSE of all with RMSE of the model using only clear-sky index persistence [118,119] provides prediction skill or skill score (SS). In addition to this, the comparison of the deep hybrid SCLC model with other comparative models was done using RMSE ratio (RMSEr) [120]. The models used have very lower SS and RMSEss than the deep hybrid SCLC model (Table 13 and Table 14).

Every station's data has four seasons with calculations for all models. Fig. 17 shows all metrics. Here also the SCLC model shows the best performance with lower RRMSE, RMAE, and APB (spring, summer, autumn, and winter) and higher WI, NSE, and KGE compared to DNN, DBN, ANN, and MARS model. Additionally, the deep hybrid SCLC model produces the less value of RMSE in season of spring ($\approx$ 2.171 $MJm^{-2}day^{-1}$), followed by Autumn ($\approx$ 2.334 $MJm^{-2}day^{-1}$), Summer ($\approx$ 2.451 $MJm^{-2}day^{-1}$), and Winter ($\approx$ 2.734 $MJm^{-2}day^{-1}$) (Fig. 18). Hence, it can be contended that the deep hybrid SCLC model can be deemed suitable for seasonal *GSR* prediction.

As final discussion note, it is possible to see how using statistical metrics and diagnostic plots, the proposed SCLC model has been validated for effectiveness and reliability. The results obtained can be analysed in terms of different assessments, including MAE, RMSE, and *r*. The results obtained showed a high value of *r* metric, and low RMSE and MAE, as can be seen in the table above. Thus, the proposed SCLC presents considerable improvements over the rest of the models analysed for comparison. Furthermore, the SCLC is not only able to significantly improve the accuracy of *GSR* prediction, but also ensure the highest prediction accuracy at different sites, maintaining a high level of performance in all them, with values of $r > 0.9$ in all cases. In detail, compared with alternative ML approaches such as CLSTM, DNN, ANN, SADE-ELM, and RFR, the RRMSE of the proposed SCLC algorithm is improved by 9%, 13%, 63%, 22%, and 115%, respectively for Barunggam Solar Farm. Additionally, the proposed hybrid method

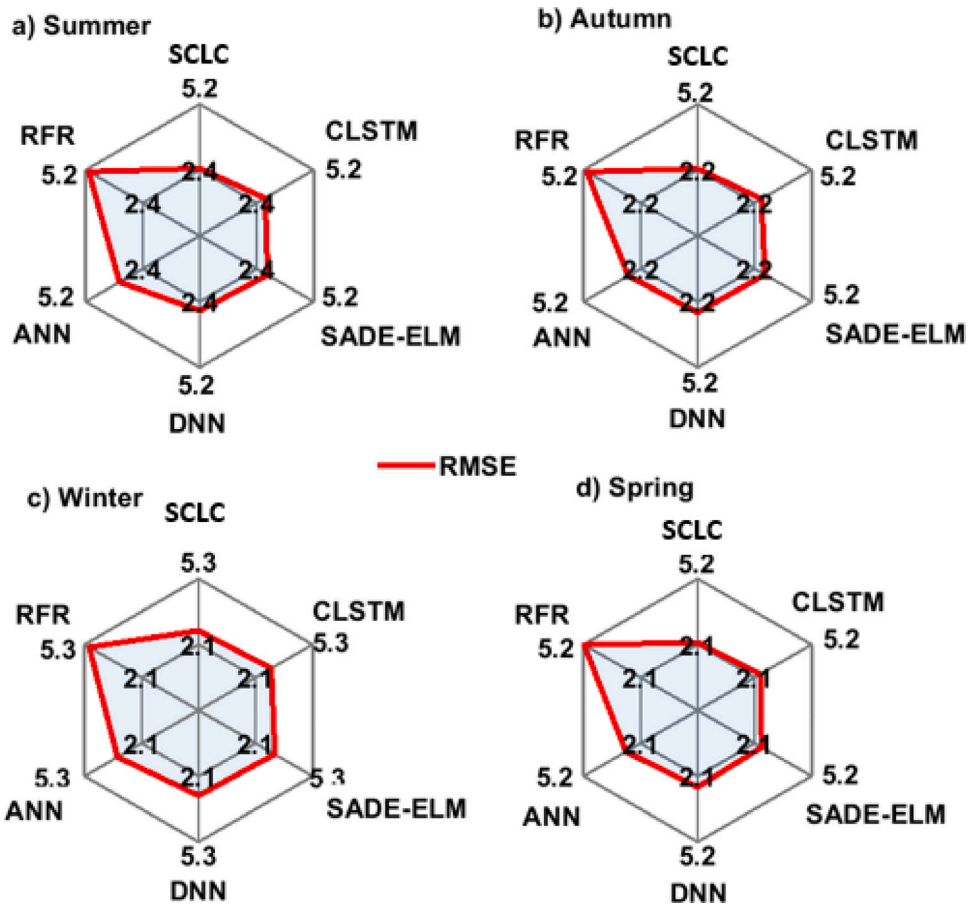

Fig. 18. Performance check of deep hybrid SCLC with others in terms of root mean square error (RMSE) (Seasonal). (Note: Model Nomenclature are in Tables 3–5).

Table 13
SCLC model score metrics as well vs. competitive models for the test phase.

Solar energy farms	SCLC	CLSTM	SADE-ELM	DNN	ANN	RFR
Barunggam Solar	**0.728**	0.679	0.596	0.655	0.276	0.261
Cameby Solar	**0.719**	0.653	0.582	0.621	0.639	0.488
Cape York Solar Storage	**0.582**	0.489	0.446	0.512	0.460	0.450
Chinchilla Solar	**0.731**	0.651	0.597	0.610	0.395	0.352
Clermont Solar	**0.697**	0.631	0.623	0.661	0.627	0.215
Sun Metals Solar	**0.613**	0.525	0.521	0.429	0.346	0.315

Table 14
SCLC model performance vs. all benchmark models for the testing period as shown by the root mean square error ratio (RMSEss).

Predictive models	SCLC	CLSTM	SADE-ELM	DNN	ANN	RFR
SCLC		**1.226**	**1.238**	**1.474**	**1.687**	**2.554**
CLSTM			1.010	1.202	1.377	2.084
SADE-ELM				1.191	1.363	2.064
DNN					1.145	1.733
ANN						1.514

achieved high performance on *GSR* prediction with the high value of KGE (≈ 0.888), GPI (≈ 1.199), and the low value of APB (≈ 9.035). The seasonal analysis of the results obtained has also shown the superior performance of the proposed SCLC versus alternative ML approaches in all cases examined.

It is remarkable that the performance of the hybrid DNN-based methods is significantly better than that by ML-based methods or simple DNNs, in all the metrics evaluated (both SCLC and the CLSTM reach the highest positions along the different evaluated solar farms). The same trend is observed in recent state-of-the-art works. For instance, in [69] the authors train two hybrid DNN-based methods: (a) CNN-ANN and (b) CNN-LSTM-ANN, and compare with ML methods in GSR prediction in different areas of Africa. The authors report an improvement of performance of hybrid approaches versus simple ML methods. No comparison has been developed regarding to hybrid DNN-based methods. Also in [73] a hybrid CNN-SVM has been evaluated, and its reported an improvement of performance versus ML methods and even pure recurrent DNNs, such as LSTMs. The combination of DNNs together with traditional ensemble methods, such as RF or XGRBoost, has also shown to be an efficient hybrid DNN-based model for radiation prediction [76]. Thus, note that hybrid DNN-based methods have recently obtained extremely good results in GSR prediction problems, significantly outperforming single ML and DNN methods.

4. Conclusions

In this paper we have developed a new deep learning-based hybrid model able to simulate the *GSR* across six solar farms considered in Queensland, Australia. The proposed system is formed by the integration of a CNN, LSTM, and finally, another CNN algorithm, thus making the overall hybrid SCLC-based predictive model. The Slime

Mould Algorithm (SMA) screens out key optimal predictive features (in terms of best input variables). To validate the proposed SCLC prediction model, five different well-established AI models (*i.e.*, CLSTM, DNN, ANN, SADE-ELM, RFR) were also implemented and compared with the proposed deep hybrid approach.

This research shows that, by combining the strengths of two DL methods (CNN and LSTM), the resulting approach obtained results superior than those by different benchmark methods considered, in terms of *GSR* prediction accuracy, forecasting speed and low volatility of prediction results. The results obtained showed an excellent adaptability to the problem of solar radiation prediction, as can be seen by comparing the results in the six solar farms considered, with excellent performance metrics ($r > 0.9$ in all cases), and improvements over alternative approaches > 10%. These results show that proposed hybrid DL algorithm is able to carry out an efficient information fusion and processing of ground-based variables and data from GCM, leading to extremely good results in the prediction of solar radiation at all study sites in Queensland, Australia.

Further improvements in the DL methodology could incorporate different design of predictor data decomposition methods, such as wavelet analysis and empirical mode decomposition [50,129,130] to screen best features using the SMA or other feature selection inputs, prior to emulating the global solar radiation, wind speed, air quality and other variables of interest. Finally, note that, in spite of the good performance of hybrid DNN models in GSR prediction, such as the one proposed in this work, there is not a comprehensive comparison of DNN-based hybrid approaches which shows the specific behaviour of different DNN-based combinations in different GSR prediction scenarios. A future line of research should fill this gap by carrying out such an experimental comparison.

CRediT authorship contribution statement

Sujan Ghimire: Data Curation, Methodology, Software, Validation, Visualization, Writing, Reviewing, Conceptualization, Investigation. **Ravinesh C. Deo:** Methodology, Visualization, Writing, Reviewing, Investigation, Conceptualization, Supervision. **David Casillas-Pérez:** Writing – review & editing, Visualization, Methodology, Conceptualization, Investigation. **Sancho Salcedo-Sanz:** Writing – review & editing, Visualization, Conceptualization, Methodology, Investigation. **Ekta Sharma:** Writing – review & editing, Investigation. **Mumtaz Ali:** Writing – review & editing, Investigation.

Declaration of competing interest

The authors declare that they have no known competing financial interests or personal relationships that could have appeared to influence the work reported in this paper.

Data availability

Supervised ML methods have been trained from Long Paddock SILO database.

Acknowledgements

We greatly acknowledge these for the data (i) Queensland Climate Change Centre of Excellence (QCCCE), a part of the Department of Science, Information Technology, Innovation, and the Arts (DSITIA) (ii) the Centre for Environmental Data Analysis (CEDA) as a server for the CMIP5 project's GCM output collection for CSIRO-BOM ACCESS1-0, MOHC Hadley-GEM2-CC and the MRI MRI-CGCM3. Partial support of this study is through the project PID2020-115454GB-C21 of the Spanish Ministry of Science and Innovation (MICINN).

References

[1] J. Fan, L. Wu, X. Ma, H. Zhou, F. Zhang, Hybrid support vector machines with heuristic algorithms for prediction of daily diffuse solar radiation in air-polluted regions, Renew. Energy 145 (2020) 2034–2045.

[2] N. Yimen, L. Monkam, D. Tcheukam-Toko, B. Musa, R. Abang, L.F. Fombe, S. Abbasoglu, M. Dagbasi, Optimal design and sensitivity analysis of distributed biomass-based hybrid renewable energy systems for rural electrification: Case study of different photovoltaic/wind/battery-integrated options in Babadam, Northern Cameroon, IET Renew. Power Gener. (2021).

[3] B. Musa, N. Yimen, S.I. Abba, H.H. Adun, M. Dagbasi, Multi-state load demand forecasting using hybridized support vector regression integrated with optimal design of off-grid energy systems—A metaheuristic approach, Processes 9 (7) (2021) 1166.

[4] M. Mukhtar, B. Ameyaw, N. Yimen, Q. Zhang, O. Bamisile, H. Adun, M. Dagbasi, Building retrofit and energy conservation/efficiency review: A techno-environ-economic assessment of heat pump system retrofit in housing stock, Sustainability 13 (2) (2021) 983.

[5] F.J. Rodríguez-Benítez, C. Arbizu-Barrena, J. Huertas-Tato, R. Aler-Mur, I. Galván-León, D. Pozo-Vázquez, A short-term solar radiation forecasting system for the Iberian Peninsula. Part 1: Models description and performance assessment, Sol. Energy 195 (2020) 396–412.

[6] A. Khanlari, A. Sözen, C. Şirin, A.D. Tuncer, A. Gungor, Performance enhancement of a greenhouse dryer: Analysis of a cost-effective alternative solar air heater, J. Cleaner Prod. 251 (2020) 119672.

[7] S.A. Kalogirou, Solar Energy Engineering: Processes and Systems, Academic Press, 2013.

[8] A. Khanlari, A. Sözen, F. Afshari, C. Şirin, A.D. Tuncer, A. Gungor, Drying municipal sewage sludge with v-groove triple-pass and quadruple-pass solar air heaters along with testing of a solar absorber drying chamber, Sci. Total Environ. 709 (2020) 136198.

[9] N. Yimen, M. Dagbasi, Multi-attribute decision-making: Applying a modified Brown–Gibson model and RETScreen software to the optimal location process of utility-scale photovoltaic plants, Processes 7 (8) (2019) 505.

[10] U. Ağbulut, A.E. Gürel, A. Ergün, I. Ceylan, Performance assessment of a V-trough photovoltaic system and prediction of power output with different machine learning algorithms, J. Cleaner Prod. 268 (2020) 122269.

[11] U. Ağbulut, A.E. Gürel, Y. Biçen, Prediction of daily global solar radiation using different machine learning algorithms: Evaluation and comparison, Renew. Sustain. Energy Rev. 135 (2021) 110114.

[12] N. Dong, J.-F. Chang, A.-G. Wu, Z.-K. Gao, A novel convolutional neural network framework based solar irradiance prediction method, Int. J. Electr. Power Energy Syst. 114 (2020) 105411.

[13] B. Jahani, Y. Dinpashoh, A.R. Nafchi, Evaluation and development of empirical models for estimating daily solar radiation, Renew. Sustain. Energy Rev. 73 (2017) 878–891.

[14] J. Fan, B. Chen, L. Wu, F. Zhang, X. Lu, Y. Xiang, Evaluation and development of temperature-based empirical models for estimating daily global solar radiation in humid regions, Energy 144 (2018) 903–914.

[15] J.-L. Chen, L. He, H. Yang, M. Ma, Q. Chen, S.-J. Wu, Z.-l. Xiao, Empirical models for estimating monthly global solar radiation: A most comprehensive review and comparative case study in China, Renew. Sustain. Energy Rev. 108 (2019) 91–111.

[16] B. Jamil, E. Bellos, Development of empirical models for estimation of global solar radiation exergy in India, J. Cleaner Prod. 207 (2019) 1–16.

[17] M. Bellaoui, K. Bouchouicha, I. Oulimar, Estimation of daily global solar radiation based on MODIS satellite measurements: The case study of adrar region (Algeria), Measurement 183 (2021) 109802.

[18] R. Chang, L. Bai, C.-H. Hsu, Solar power generation prediction based on deep learning, Sustain. Energy Technol. Assess. 47 (2021) 101354.

[19] Y. Feng, D. Gong, Q. Zhang, S. Jiang, L. Zhao, N. Cui, Evaluation of temperature-based machine learning and empirical models for predicting daily global solar radiation, Energy Convers. Manage. 198 (2019) 111780.

[20] A. Khosravi, R.O. Nunes, M.E.H. Assad, L. Machado, Comparison of artificial intelligence methods in estimation of daily global solar radiation, J. Cleaner Prod. 194 (2018) 342–358.

[21] S.S. Sharifi, V. Rezaverdinejad, V. Nourani, Estimation of daily global solar radiation using wavelet regression, ANN, GEP and empirical models: A comparative study of selected temperature-based approaches, J. Atmos. Sol.-Terr. Phys. 149 (2016) 131–145.

[22] Y. Jiang, Prediction of monthly mean daily diffuse solar radiation using artificial neural networks and comparison with other empirical models, Energy Policy 36 (10) (2008) 3833–3837.

[23] F. Zhang, J.-R. Yan, J. Li, K. Wu, H. Iwabuchi, Y.-N. Shi, A new radiative transfer method for solar radiation in a vertically internally inhomogeneous medium, J. Atmos. Sci. 75 (1) (2018) 41–55.

[24] I.M. Galván, J. Huertas-Tato, F.J. Rodríguez-Benítez, C. Arbizu-Barrena, D. Pozo-Vázquez, R. Aler, Evolutionary-based prediction interval estimation by blending solar radiation forecasting models using meteorological weather types, Appl. Soft Comput. (2021) 107531.

[25] H. Gamarro, J.E. Gonzalez, L.E. Ortiz, On the assessment of a numerical weather prediction model for solar photovoltaic power forecasts in cities, J. Energy Resour. Technol. 141 (6) (2019).

[26] C. Voyant, M. Muselli, C. Paoli, M.-L. Nivet, Numerical weather prediction (NWP) and hybrid ARMA/ANN model to predict global radiation, Energy 39 (1) (2012) 341–355.

[27] K. Yang, T. Koike, B. Ye, Improving estimation of hourly, daily, and monthly solar radiation by importing global data sets, Agricult. Forest Meteorol. 137 (1–2) (2006) 43–55.

[28] S. Salcedo-Sanz, P. Ghamisi, M. Piles, M. Werner, L. Cuadra, A. Moreno-Martínez, E. Izquierdo-Verdiguier, J. Muñoz-Marí, A. Mosavi, G. Camps-Valls, Machine learning information fusion in Earth observation: A comprehensive review of methods, applications and data sources, Inf. Fusion 63 (2020) 256–272.

[29] O. García-Hinde, G. Terrén-Serrano, M. Hombrados-Herrera, V. Gómez-Verdejo, S. Jiménez-Fernández, C. Casanova-Mateo, J. Sanz-Justo, M. Martínez-Ramón, S. Salcedo-Sanz, Evaluation of dimensionality reduction methods applied to numerical weather models for solar radiation forecasting, Eng. Appl. Artif. Intell. 69 (2018) 157–167.

[30] A. Hammer, D. Heinemann, C. Hoyer, R. Kuhlemann, E. Lorenz, R. Müller, H.G. Beyer, Solar energy assessment using remote sensing technologies, Remote Sens. Environ. 86 (3) (2003) 423–432.

[31] H. Sun, D. Yan, N. Zhao, J. Zhou, Empirical investigation on modeling solar radiation series with ARMA-GARCH models, Energy Convers. Manage. 92 (2015) 385–395.

[32] K. Gairaa, A. Khellaf, Y. Messlem, F. Chellali, Estimation of the daily global solar radiation based on Box–Jenkins and ANN models: A combined approach, Renew. Sustain. Energy Rev. 57 (2016) 238–249.

[33] M. Ghofrani, M. Ghayekhloo, R. Azimi, A novel soft computing framework for solar radiation forecasting, Appl. Soft Comput. 48 (2016) 207–216.

[34] A. Jadidi, R. Menezes, N. De Souza, A.C. de Castro Lima, A hybrid GA–MLPNN model for one-hour-ahead forecasting of the global horizontal irradiance in Elizabeth city, North Carolina, Energies 11 (10) (2018) 2641.

[35] W. Sun, Y. Wang, Short-term wind speed forecasting based on fast ensemble empirical mode decomposition, phase space reconstruction, sample entropy and improved back-propagation neural network, Energy Convers. Manage. 157 (2018) 1–12.

[36] J. Cao, X. Lin, Application of the diagonal recurrent wavelet neural network to solar irradiation forecast assisted with fuzzy technique, Eng. Appl. Artif. Intell. 21 (8) (2008) 1255–1263.

[37] H. Jiang, A novel approach for forecasting global horizontal irradiance based on sparse quadratic RBF neural network, Energy Convers. Manage. 152 (2017) 266–280.

[38] S. Salcedo-Sanz, R.C. Deo, L. Cornejo-Bueno, C. Camacho-Gómez, S. Ghimire, An efficient neuro-evolutionary hybrid modelling mechanism for the estimation of daily global solar radiation in the sunshine state of Australia, Appl. Energy 209 (2018) 79–94.

[39] D. Guijo-Rubio, A.M. Durán-Rosal, P.A. Gutiérrez, A.M. Gómez-Orellana, C. Casanova-Mateo, J. Sanz-Justo, S. Salcedo-Sanz, C. Hervás-Martínez, Evolutionary artificial neural networks for accurate solar radiation prediction, Energy 210 (2020) 118374.

[40] M.M. Lotfinejad, R. Hafezi, M. Khanali, S.S. Hosseini, M. Mehrpooya, S. Shamshirband, A comparative assessment of predicting daily solar radiation using bat neural network (BNN), generalized regression neural network (GRNN), and neuro-fuzzy (NF) system: A case study, Energies 11 (5) (2018) 1188.

[41] S. Salcedo-Sanz, C. Casanova-Mateo, A. Pastor-Sánchez, M. Sánchez-Girón, Daily global solar radiation prediction based on a hybrid coral reefs optimization–Extreme learning machine approach, Sol. Energy 105 (2014) 91–98.

[42] A. Aybar-Ruiz, S. Jiménez-Fernández, L. Cornejo-Bueno, C. Casanova-Mateo, J. Sanz-Justo, P. Salvador-González, S. Salcedo-Sanz, A novel grouping genetic algorithm–extreme learning machine approach for global solar radiation prediction from numerical weather models inputs, Sol. Energy 132 (2016) 129–142.

[43] S. Salcedo-Sanz, S. Jiménez-Fernández, A. Aybar-Ruíz, C. Casanova-Mateo, J. Sanz-Justo, R. García-Herrera, A CRO-species optimization scheme for robust global solar radiation statistical downscaling, Renew. Energy 111 (2017) 63–76.

[44] S. Ghimire, R.C. Deo, N.J. Downs, N. Raj, Self-adaptive differential evolutionary extreme learning machines for long-term solar radiation prediction with remotely-sensed MODIS satellite and reanalysis atmospheric products in solar-rich cities, Remote Sens. Environ. 212 (2018) 176–198.

[45] J. Chen, W. Zhu, Q. Yu, Estimating half-hourly solar radiation over the continental united states using GOES-16 data with iterative random forest, Renew. Energy 178 (2021) 916–929.

[46] L. Benali, G. Notton, A. Fouilloy, C. Voyant, R. Dizene, Solar radiation forecasting using artificial neural network and random forest methods: Application to normal beam, horizontal diffuse and global components, Renew. Energy 132 (2019) 871–884.

[47] J.-L. Chen, H.-B. Liu, W. Wu, D.-T. Xie, Estimation of monthly solar radiation from measured temperatures using support vector machines–A case study, Renew. Energy 36 (1) (2011) 413–420.

[48] J.-L. Chen, G.-S. Li, Evaluation of support vector machine for estimation of solar radiation from measured meteorological variables, Theor. Appl. Climatol. 115 (3) (2014) 627–638.

[49] M. Alrashidi, M. Alrashidi, S. Rahman, Global solar radiation prediction: Application of novel hybrid data-driven model, Appl. Soft Comput. 112 (2021) 107768.

[50] R. Deo, X. Wen, F. Qi, A wavelet-coupled support vector machine model for forecasting global incident solar radiation using limited meteorological dataset, Appl. Energy 168 (2016) 568–593.

[51] S. Salcedo-Sanz, C. Casanova-Mateo, J. Muñoz-Marí, G. Camps-Valls, Prediction of daily global solar irradiation using temporal Gaussian processes, IEEE Geosci. Remote Sens. Lett. 11 (11) (2014) 1936–1940.

[52] J. Piri, O. Kisi, Modelling solar radiation reached to the Earth using ANFIS, NN-ARX, and empirical models (Case studies: Zahedan and Bojnurd stations), J. Atmos. Sol.-Terr. Phys. 123 (2015) 39–47.

[53] L. Cornejo-Bueno, C. Casanova-Mateo, J. Sanz-Justo, S. Salcedo-Sanz, Machine learning regressors for solar radiation estimation from satellite data, Sol. Energy 183 (2019) 768–775.

[54] S. Ghimire, R.C. Deo, N.J. Downs, N. Raj, Global solar radiation prediction by ANN integrated with European centre for medium range weather forecast fields in solar rich cities of Queensland Australia, J. Cleaner Prod. 216 (2019) 288–310.

[55] A.E. Gürel, U. Ağbulut, Y. Biçen, Assessment of machine learning, time series, response surface methodology and empirical models in prediction of global solar radiation, J. Cleaner Prod. 277 (2020) 122353.

[56] V.H. Quej, J. Almorox, J.A. Arnaldo, L. Saito, ANFIS, SVM and ANN soft-computing techniques to estimate daily global solar radiation in a warm sub-humid environment, J. Atmos. Sol.-Terr. Phys. 155 (2017) 62–70.

[57] A.G. Salman, B. Kanigoro, Y. Heryadi, Weather forecasting using deep learning techniques, in: 2015 International Conference on Advanced Computer Science and Information Systems, ICACSIS, Ieee, 2015, pp. 281–285.

[58] X. Qing, Y. Niu, Hourly day-ahead solar irradiance prediction using weather forecasts by LSTM, Energy 148 (2018) 461–468.

[59] M. Mishra, P.B. Dash, J. Nayak, B. Naik, S.K. Swain, Deep learning and wavelet transform integrated approach for short-term solar PV power prediction, Measurement 166 (2020) 108250.

[60] S. Ghimire, R.C. Deo, N. Raj, J. Mi, Deep learning neural networks trained with MODIS satellite-derived predictors for long-term global solar radiation prediction, Energies 12 (12) (2019) 2407.

[61] K. Yan, H. Shen, L. Wang, H. Zhou, M. Xu, Y. Mo, Short-term solar irradiance forecasting based on a hybrid deep learning methodology, Information 11 (1) (2020) 32.

[62] O. Bamisile, A. Oluwasanmi, C. Ejiyi, N. Yimen, S. Obiora, Q. Huang, Comparison of machine learning and deep learning algorithms for hourly global/diffuse solar radiation predictions, Int. J. Energy Res. (2021).

[63] H. Zang, L. Cheng, T. Ding, K.W. Cheung, M. Wang, Z. Wei, G. Sun, Application of functional deep belief network for estimating daily global solar radiation: A case study in China, Energy 191 (2020) 116502.

[64] T. Peng, C. Zhang, J. Zhou, M.S. Nazir, An integrated framework of bi-directional long-short term memory (BiLSTM) based on sine cosine algorithm for hourly solar radiation forecasting, Energy 221 (2021) 119887.

[65] W. Bendali, I. Saber, B. Bourachdi, M. Boussetta, Y. Mourad, Deep learning using genetic algorithm optimization for short term solar irradiance forecasting, in: 2020 Fourth International Conference on Intelligent Computing in Data Sciences, ICDS, IEEE, 2020, pp. 1–8.

[66] M. Abdel-Nasser, K. Mahmoud, M. Lehtonen, Reliable solar irradiance forecasting approach based on choquet integral and deep LSTMs, IEEE Trans. Ind. Inf. 17 (3) (2020) 1873–1881.

[67] S. Ziyabari, L. Du, S. Biswas, A spatio-temporal hybrid deep learning architecture for short-term solar irradiance forecasting, in: 2020 47th IEEE Photovoltaic Specialists Conference, PVSC, IEEE, 2020, pp. 0833–0838.

[68] C.S. Lai, C. Zhong, K. Pan, W.W.Y. Ng, L.L. Lai, A deep learning based hybrid method for hourly solar radiation forecasting, Expert Syst. Appl. 177 (2021) 114941.

[69] M. Mukhtar, A. Oluwasanmi, N. Yimen, Z. Qinxiu, C.C. Ukwuoma, B. Ezurike, O. Bamisile, Development and comparison of two novel hybrid neural network models for hourly solar radiation prediction, Appl. Sci. 12 (3) (2022) 1435.

[70] H. Acikgoz, A novel approach based on integration of convolutional neural networks and deep feature selection for short-term solar radiation forecasting, Appl. Energy 305 (2022) 117912, http://dx.doi.org/10.1016/j.apenergy.2021.117912, URL https://www.sciencedirect.com/science/article/pii/S0306261921012241.

[71] S. Ghimire, R.C. Deo, D. Casillas-Pérez, S. Salcedo-Sanz, Improved complete ensemble empirical mode decomposition with adaptive noise deep residual model for short-term multi-step solar radiation prediction, Renew. Energy 190 (2022) 408–424.

[72] H. Jiang, N. Lu, J. Qin, W. Tang, L. Yao, A deep learning algorithm to estimate hourly global solar radiation from geostationary satellite data, Renew. Sustain. Energy Rev. 114 (2019) 109327.

[73] S. Ghimire, B. Bhandari, D. Casillas-Pérez, R.C. Deo, S. Salcedo-Sanz, Hybrid deep CNN-SVR algorithm for solar radiation prediction problems in queensland, Australia, Eng. Appl. Artif. Intell. 112 (2022) 104860, http://dx.doi.org/10.1016/j.engappai.2022.104860, URL https://www.sciencedirect.com/science/article/pii/S0952197622001099.
[74] S. Ghimire, T. Nguyen-Huy, R.C. Deo, D. Casillas-Pérez, S. Salcedo-Sanz, Efficient daily solar radiation prediction with deep learning 4-phase convolutional neural network, dual stage stacked regression and support vector machine CNN-REGST hybrid model, Sustai. Mater. Technol. 32 (2022) e00429, http://dx.doi.org/10.1016/j.susmat.2022.e00429, URL https://www.sciencedirect.com/science/article/pii/S2214993722000434.
[75] D. Cannizzaro, A. Aliberti, L. Bottaccioli, E. Macii, A. Acquaviva, E. Patti, Solar radiation forecasting based on convolutional neural network and ensemble learning, Expert Syst. Appl. 181 (2021) 115167.
[76] S. Ghimire, R.C. Deo, D. Casillas-Pérez, S. Salcedo-Sanz, Boosting solar radiation predictions with global climate models, observational predictors and hybrid deep-machine learning algorithms, Appl. Energy 316 (2022) 119063, http://dx.doi.org/10.1016/j.apenergy.2022.119063, URL https://www.sciencedirect.com/science/article/pii/S0306261922004585.
[77] M. Abadi, P. Barham, J. Chen, Z. Chen, A. Davis, J. Dean, M. Devin, S. Ghemawat, G. Irving, M. Isard, et al., Tensorflow: A system for large-scale machine learning, in: 12th {USENIX} Symposium on Operating Systems Design and Implementation, OSDI 16, 2016, pp. 265–283.
[78] Works DoEaP, Powering Queensland plan: An integrated energy strategy for the state; Queensland government, 2021.
[79] Works DoEaP, Achieving our renewable energy targets. Queensland government, 2021.
[80] G. Stone, R. Dalla Pozza, J. Carter, G. McKeon, Long paddock: Climate risk and grazing information for Australian rangelands and grazing communities, Rangel. J. 41 (3) (2019) 225–232.
[81] Centre for environmental data analysis. CEDA archive, 2020.
[82] The Commonwealth Scientific and Industrial Research Organisation; Bureau of Meteorology, WCRP CMIP5: The CSIRO-BOM Team ACCESS1-0 Model Output Collection, Centre for Environmental Data Analysis, 2017.
[83] Met Office Hadley Centre, WCRP CMIP5: Met Office Hadley Centre (MOHC) HadGEM2-CC Model Output Collection, Centre for Environmental Data Analysis, 2012.
[84] Meteorological Research Institute of the Korean Meteorological Administration, WCRP CMIP5: Meteorological research institute of kma MRI-CGCM3 model output collection, Centre for Environmental Data Analysis, 2013.
[85] S. Salcedo-Sanz, L. Cornejo-Bueno, L. Prieto, D. Paredes, R. García-Herrera, Feature selection in machine learning prediction systems for renewable energy applications, Renew. Sustain. Energy Rev. 90 (2018) 728–741.
[86] M. Almaraashi, Investigating the impact of feature selection on the prediction of solar radiation in different locations in Saudi Arabia, Appl. Soft Comput. 66 (2018) 250–263.
[87] M. Castangia, A. Aliberti, L. Bottaccioli, E. Macii, E. Patti, A compound of feature selection techniques to improve solar radiation forecasting, Expert Syst. Appl. 178 (2021) 114979.
[88] S. Li, H. Chen, M. Wang, A.A. Heidari, S. Mirjalili, Slime mould algorithm: A new method for stochastic optimization, Future Gener. Comput. Syst. 111 (2020) 300–323.
[89] N.S. Altman, An introduction to kernel and nearest-neighbor nonparametric regression, Amer. Statist. 46 (3) (1992) 175–185.
[90] G. Vashishtha, S. Chauhan, M. Singh, R. Kumar, Bearing defect identification by swarm decomposition considering permutation entropy measure and opposition-based slime mould algorithm, Measurement 178 (2021) 109389.
[91] Y. Sun, G. Szűcs, A.R. Brandt, Solar PV output prediction from video streams using convolutional neural networks, Energy Environ. Sci. 11 (7) (2018) 1811–1818.
[92] J. Gu, Z. Wang, J. Kuen, L. Ma, A. Shahroudy, B. Shuai, T. Liu, X. Wang, G. Wang, J. Cai, et al., Recent advances in convolutional neural networks, Pattern Recognit. 77 (2018) 354–377.
[93] D.-X. Zhou, Universality of deep convolutional neural networks, Appl. Comput. Harmon. Anal. 48 (2) (2020) 787–794.
[94] S. Hochreiter, J. Schmidhuber, Long short-term memory, Neural Comput. 9 (8) (1997) 1735–1780.
[95] J.-M. Yeom, R.C. Deo, J.F. Adamowski, S. Park, C.-S. Lee, Spatial mapping of short-term solar radiation prediction incorporating geostationary satellite images coupled with deep convolutional LSTM networks for South Korea, Environ. Res. Lett. 15 (9) (2020) 094025.
[96] A. Gensler, J. Henze, B. Sick, N. Raabe, Deep learning for solar power forecasting—An approach using AutoEncoder and LSTM neural networks, in: 2016 IEEE International Conference on Systems, Man, and Cybernetics, SMC, IEEE, 2016, pp. 002858–002865.
[97] S. Srivastava, S. Lessmann, A comparative study of LSTM neural networks in forecasting day-ahead global horizontal irradiance with satellite data, Sol. Energy 162 (2018) 232–247.
[98] A. Graves, Generating sequences with recurrent neural networks, 2013, arXiv preprint arXiv:1308.0850.
[99] S. Ghimire, Z.M. Yaseen, A.A. Farooque, R.C. Deo, J. Zhang, X. Tao, Streamflow prediction using an integrated methodology based on convolutional neural network and long short-term memory networks, Sci. Rep. 11 (1) (2021) 1–26.
[100] F. Chollet, et al., Keras (2015), 2017.
[101] P. Goldsborough, A tour of tensorflow, 2016, arXiv preprint arXiv:1610.01178.
[102] H. Xie, L. Zhang, C.P. Lim, Evolving CNN-LSTM models for time series prediction using enhanced grey wolf optimizer, IEEE Access 8 (2020) 161519–161541.
[103] N. Reimers, I. Gurevych, Optimal hyperparameters for deep LSTM-networks for sequence labeling tasks, 2017, arXiv preprint arXiv:1707.06799.
[104] G. Xie, A. Shangguan, R. Fei, W. Ji, W. Ma, X. Hei, Motion trajectory prediction based on a CNN-LSTM sequential model, Sci. China Inf. Sci. 63 (11) (2020) 1–21.
[105] I. Priyadarshini, C. Cotton, A novel LSTM–CNN–grid search-based deep neural network for sentiment analysis, J. Supercomput. (2021) 1–22.
[106] S. Cavalli, M. Amoretti, CNN-based multivariate data analysis for bitcoin trend prediction, Appl. Soft Comput. 101 (2021) 107065.
[107] M. Čokina, V. Maslej-Krešňáková, P. Butka, Š. Parimucha, Automatic classification of eclipsing binary stars using deep learning methods, Astron. Comput. 36 (2021) 100488.
[108] D.P. Kingma, J. Ba, Adam: A method for stochastic optimization, 2014, arXiv preprint arXiv:1412.6980.
[109] Y. Qi, Q. Li, H. Karimian, D. Liu, A hybrid model for spatiotemporal forecasting of PM2. 5 based on graph convolutional neural network and long short-term memory, Sci. Total Environ. 664 (2019) 1–10.
[110] Y. Sun, Z. Xie, Y. Chen, X. Huang, Q. Hu, Solar wind speed prediction with two-dimensional attention mechanism, Space Weather 19 (7) (2021).
[111] S. Tiwari, R. Sabzehgar, M. Rasouli, Short term solar irradiance forecast based on image processing and cloud motion detection, in: 2019 IEEE Texas Power and Energy Conference, TPEC, IEEE, 2019, pp. 1–6.
[112] J.-D. Jang, A.A. Viau, F. Anctil, Neural network estimation of air temperatures from AVHRR data, Int. J. Remote Sens. 25 (21) (2004) 4541–4554.
[113] N. Lu, J. Qin, K. Yang, J. Sun, A simple and efficient algorithm to estimate daily global solar radiation from geostationary satellite data, Energy 36 (5) (2011) 3179–3188.
[114] S. Sun, H. Qiao, Y. Wei, S. Wang, A new dynamic integrated approach for wind speed forecasting, Appl. Energy 197 (2017) 151–162.
[115] F.X. Diebold, R.S. Mariano, Comparing predictive accuracy, J. Bus. Econom. Statist. 20 (1) (2002) 134–144.
[116] M. Costantini, C. Pappalardo, Combination of Forecast Methods using Encompassing Tests: An Algorithm-Based Procedure, Tech. Rep., Reihe Ökonomie/Economics Series, 2008.
[117] K.E. Taylor, Summarizing multiple aspects of model performance in a single diagram, J. Geophys. Res.: Atmos. 106 (D7) (2001) 7183–7192.
[118] R. Marquez, C.F.M. Coimbra, Proposed metric for evaluation of solar forecasting models, J. Sol. Energy Eng. 135 (1) (2013) 011016.
[119] S. Salcedo-Sanz, D. Casillas-Pérez, J. Del Ser, C. Casanova-Mateo, L. Cuadra, M. Piles, G. Camps-Valls, Persistence in complex systems, Phys. Rep. 957 (2022) 1–73.
[120] D. Yang, S. Alessandrini, J. Antonanzas, F. Antonanzas-Torres, V. Badescu, H.G. Beyer, R. Blaga, J. Boland, J.M. Bright, C.F.M. Coimbra, et al., Verification of deterministic solar forecasts, Sol. Energy 210 (2020) 20–37.
[121] T. Pan, S. Wu, E. Dai, Y. Liu, Estimating the daily global solar radiation spatial distribution from diurnal temperature ranges over the Tibetan Plateau in China, Appl. Energy 107 (2013) 384–393.
[122] C.J. Willmott, K. Matsuura, Advantages of the mean absolute error (MAE) over the root mean square error (RMSE) in assessing average model performance, Clim. Res. 30 (1) (2005) 79–82.
[123] J.E. Nash, J.V. Sutcliffe, River flow forecasting through conceptual models part I—A discussion of principles, J. Hydrol. 10 (3) (1970) 282–290.
[124] D.R. Legates, G.J. McCabe Jr., Evaluating the use of "goodness-of-fit" measures in hydrologic and hydroclimatic model validation, Water Resour. Res. 35 (1) (1999) 233–241.
[125] M. Despotovic, V. Nedic, D. Despotovic, S. Cvetanovic, Review and statistical analysis of different global solar radiation sunshine models, Renew. Sustain. Energy Rev. 52 (2015) 1869–1880.
[126] H.V. Gupta, H. Kling, K.K. Yilmaz, G.F. Martinez, Decomposition of the mean squared error and NSE performance criteria: Implications for improving hydrological modelling, J. Hydrol. 377 (1–2) (2009) 80–91.
[127] J. McKenzie, Mean absolute percentage error and bias in economic forecasting, Econom. Lett. 113 (3) (2011) 259–262.
[128] H. Liu, X. Mi, Y. Li, Smart deep learning based wind speed prediction model using wavelet packet decomposition, convolutional neural network and convolutional long short term memory network, Energy Convers. Manage. 166 (2018) 120–131.
[129] S. Ghimire, R.C. Deo, N. Raj, J. Mi, Wavelet-based 3-phase hybrid SVR model trained with satellite-derived predictors, particle swarm optimization and maximum overlap discrete wavelet transform for solar radiation prediction, Renew. Sustain. Energy Rev. 113 (2019) 109247.
[130] M.S. Al-Musaylh, R.C. Deo, Y. Li, J.F. Adamowski, Two-phase particle swarm optimized-support vector regression hybrid model integrated with improved empirical mode decomposition with adaptive noise for multiple-horizon electricity demand forecasting, Appl. Energy 217 (2018) 422–439.